Studies Pertaining to a Small Damping Ring for the International Linear Collider FERMILAB-TM-2272-AD-TD

Louis Emery, Kwang-Je Kim
Argonne National Accelerator Laboratory, Argonne, IL 60439

Joe Rogers
Cornell University, Ithaca, NY 14853

Shekhar Mishra, David Neuffer, K.Y. Ng, Jean-François Ostiguy, Nikolay Solyak, Aimin Xiao
Fermi National Accelerator Laboratory, Batavia, IL 60510

George D. Gollin[1], Guy Bresler, Keri Dixon, Thomas R. Junk, Jeremy B. Williams
Dept. of Physics, University of Illinois at Urbana-Champaign, Urbana, IL 61801

September 28, 2004

FERMILAB-TM-2272-AD-TD

Abstract

The size of the International Linear Collider's damping rings is dictated in part by the performance of the injection/extraction kicker. The challenges associated with a fast pulsed kicker were considered too difficult when the TESLA *Technical Design Report* was written, leading to TESLA damping rings 17 km in circumference. A number of ideas that might allow construction of smaller rings have arisen recently. Some combination of these may well eliminate damping ring bunch spacing as the primary constraint on the ring's minimum circumference.

We have been exploring one particular scheme for a small damping ring in which adequate space is provided for insertion of one of several possible kickers currently under investigation in the ILC community. In this document we report our progress on design studies for a 6.1 km circular ring and a kicker in which the Fourier decomposition of a periodic pulse is used for injection and extraction. Though our studies are ongoing, we are encouraged about the prospects for a smaller ring and summarize our efforts here.

[1] Email: g-gollin@uiuc.edu

Contents

Abstract 1
Contents 2
1. Introduction and overview 3
2. Small damping ring lattice and characteristics 4
Design Considerations 5
Circumference 5
Ring Energy 5
Damping Time and Horizontal Emittance 6
Linear Optics 7
Chromaticity Correction and Dynamic Aperture 12
Further Work 14
3. Injection and extraction optics 14
4. RF and collective effects 16
RF System 16
Optimum Coupling Coefficient 17
Detuning 17
Beam Loading 18
Impedance of the Vacuum Chamber 19
Space Charge 19
Wall impedance 21
Button BPM 21
Impedance summary 22
Single Bunch Instabilities 23
Microwave Instability 23
Transverse Mode-Coupling Instability 23
Multi-Bunch Instabilities 25
Longitudinal Coupled-Bunch Instabilities 25
Transverse Coupled-Bunch Instabilities 25
Electron Clouds and Trapped Ions 26
Electron-Cloud Effect 26
Trapped Ions 27
5. Controls and instrumentation 38
Tolerances and Correction Procedures 38
Beam-Gas and Intrabeam Scattering 40
6. Fourier kicker system 41
Introduction 41
General Discussion of a Fourier-Series Kicker System 41
Mode of Operation During Extraction and Injection 46
Effect of Bunch Arrival Time Error at the Kicker 47
Effects Associated With Multiple Passes Through the Kicker 48
Summing the Fourier Components 48
Cavity Design and RF Power Requirements 55
Stability Considerations 55
7. Conclusions 59
References 59

1. Introduction and overview

The number of bunches in a beam pulse from the International Linear Collider would require an unacceptably large damping ring if the linac bunch spacing were also used inside the rings. A long linac bunch interval (340 ns in the TESLA linac design) is likely to be a feature of any L-band superconducting linear accelerator, including the ILC.

The TESLA damping ring bunch spacing was specified as 20 ns, yielding a 17 km circumference for each of the rings. Fast kickers would be used to deflect individual bunches on injection or extraction, leaving the orbits of adjacent bunches undisturbed.

The size of the rings was dictated by the anticipated performance of the kicker: a faster kicker would permit the construction of smaller rings, but the challenges associated with the design and stable operation of a faster pulsed kicker were thought to be daunting at the time the TESLA TDR was written. A number of the kicker designs required the creation of individual pulses of sufficiently short duration so that only one bunch would be influenced by a kicking impulse.

A number of ideas that might allow construction of a faster kicker, and therefore smaller damping rings, have arisen recently. Some combination of these may well eliminate the damping ring bunch spacing as the primary constraint on the ring's minimum circumference. As a result, it is appropriate to investigate in some detail an alternative damping ring design which uses a kicker that admits smaller bunch spacing.

We have been exploring one particular scheme in which adequate space in the ring is provided for insertion of any one of several possible kickers currently under investigation in the ILC community. In addition, we are studying a kicker design in which the Fourier decomposition of a periodic pulse is used for injection and extraction. Though our studies are still in progress, we are encouraged about the prospects for a smaller ring and feel it is appropriate to summarize our progress at this time.

In our model, the damping ring beam is grouped into 60 bunch trains. Each train consists of 47 bunches spaced by 6.07 ns; a gap separates the tail of each train from the head of the following train. During extraction, the last bunch from each train is ejected in the course of one orbit. As a result, the entire extraction cycle requires 47 orbits. Injection is a time-reversed version of extraction: undamped bunches are delivered to the kicker every 340 ns and are kicked on-orbit as the (new) first bunch in a train.

The lengths of inter-train gaps are chosen to present a bunch that is to be ejected to the kicker every 340 ns. The gap after the last train is slightly longer than the other (identical) inter-train gaps so that the position in a train of the kicked bunch will change after each orbit.

The total circumference of a damping ring capable of holding all 2820 bunches is 6.12 km. Some of the parameters relating to the ring and contained beam are shown in Table 1.1.

Parameter	Value
Main linac RF frequency	1.300 GHz (442 × linac bunch frequency)
Main linac bunch spacing	340 ns (1/442 of linac RF frequency)
Number of main linac bunches	2820
Number of damping ring bunch trains	60
Bunches per train	47
Inter-train gap following trains 1-59	10 damping ring bunch spacings (~60.7 ns)
Inter-train gap following train 60	11 damping ring bunch spacings (~66.8 ns)
Inter-bunch separation	~6.07 ns (main linac bunch spacing / 56)
Train length (including gap), trains 1-59	340 ns = main linac bunch spacing
Train length (including gap), train 60	~346.1 ns = 57 × bunch spacing
Damping ring orbit period	~20,406.1 ns (60 × 340 + 1 inter-bunch gap)
Damping ring orbit circumference	~6.12 km = (60 × 340 + 1 inter-bunch gap)*c*
Damping ring RF frequency	~494.1 MHz (168 × linac bunch frequency)
Kicker center frequency	~1.647 GHz (10 × 1/ DR bunch spacing)
Kicker bandwidth	±10% of center frequency

Table 1.1: Damping ring beam timing structure assumed in our studies

2. Small damping ring lattice and characteristics

The TESLA TDR's damping ring design has a circumference of 17 km in order to accommodate a 1 ms long train of 2820 bunches per linac pulse. This circumference is the minimum allowed by a state-of-the art kicker with rise and fall times of ~15 ns. However, preliminary studies suggest that it might be possible to reduce the kicker's rise time to ~5 ns, making it possible to compress a single 2820 bunch train into 60 short bunch trains comprising 47 bunches per train.

We consider here bunch spacing within a train of 6.07 ns, exactly 1/56 of the 340 ns bunch spacing in the main linac. Inter-train gaps separate adjacent trains in the ring. This gap would allow the use of a pulsed kicker with a challengingly fast rise time, but currently achievable fall time, if the kicker only acted on the last bunch in each train. This sort of injection/extraction scheme is shown in Fig. 2.1.

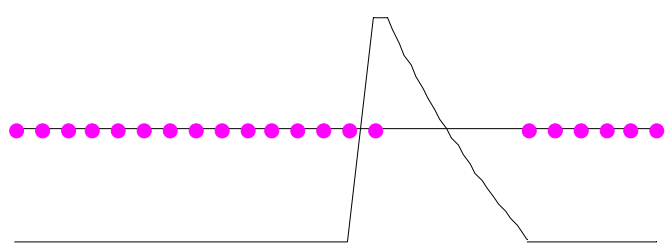

Figure 2.1: Possible injection/extraction scheme for a small damping ring using a pulsed kicker

An alternative scheme, compatible with the train structure described above would use a "Fourier kicker," in which the kick is provided by a sum of RF harmonics whose superposition creates a periodic narrow pulse.

We have assumed that the performance goals for a small damping ring are the same as those for TESLA's 17 km damping ring. Our studies include a preliminary dynamic aperture survey that assumes linear wiggler magnets. We find that a small damping ring can meet the performance goals demanded of an ILC damping ring.

Design Considerations

Circumference

We developed our damping ring lattice using the systematic approach described in a recent publication by Emma and Raubenheimer [2.1] The requirements and input parameters for the Fermilab damping ring lattice design are listed in Tables 1.1 and 2.1 [2.2]. The number of bunches per train is $N_b = (T_t - 60.7)/6.07 + 1 = 47$, the total train number is $N_t = N_{b,total} / N_b = 60$, and the circumference[2] is $C = (T_t N_t + 6.07)c = 6117.595$ m.

Number of bunches $N_{b,total}$	2820
Train to train spacing T_t ns	340
Kicker rise time $\tau_{k,r}$ ns	<6.0
Kicker fall time $\tau_{k,f}$ ns	<60
Cycle time T_c s	0.2
Injected emittance $\gamma\varepsilon_{x(y)}$ m	0.01
Horizontal extracted emittance $\gamma\varepsilon_x$ m	8×10^{-6}
Vertical extracted emittance $\gamma\varepsilon_y$ m	0.02×10^{-6}

Table 2.1: Input parameters and extracted emittance requirements for the Fermilab positron damping ring

Ring Energy

The desire to maintain high-spin polarization limits the choice of ring energy; to avoid resonances, the spin tune should be a half integer $a\gamma = n + 1/2$ where $a \approx 1.16\times10^{-3}$.

[2] The last train is 340 + 6 ns long instead of 340 ns in order to inject/extract the next bunch in the first train on successive orbits.

Taking into consideration damping time and stability, we choose E = 5.066 GeV, which makes n = 11.

Damping Time and Horizontal Emittance

Here, we assume the vertical damping time to be the same as for the TESLA design *i.e.*, τ_y = 28 ms.

The total beam storage time expressed in units of damping time is 7.2. Neglecting the contribution from the natural equilibrium emittance, the vertical emittance as a function of time is given by

$$\varepsilon = (\varepsilon_0 - \varepsilon_e)e^{-2t/\tau} + \varepsilon_e \tag{2.1}$$

In Eq. 2.1, ε_0 is the emittance at injection and $\varepsilon_{ye} = 1.44 \times 10^{-8}$ m is the equilibrium vertical emittance, whose value is determined by residual transverse coupling. The implications of this value on vertical alignment tolerances and coupling correction schemes has not been studied and will be carried out later. τ_y can be written [2.3] as shown in Eq. 2.2:

$$\tau_y = \frac{3C}{r_e c \gamma^3 I_2} = \frac{3C}{r_e c \gamma^3 \left(I_{2a} + I_{2w}\right)}. \tag{2.2}$$

Here, r_e is the classical electron radius, c is the speed of light, γ is the beam energy in units of mc^2, and

$$I_2 = \int_{dipoles} \frac{1}{\rho^2} ds = \int_{B_arc} \frac{1}{\rho^2} ds + \int_{wiggler} \frac{1}{\rho^2} ds \tag{2.2a}$$

is the second synchrotron integral over dipoles.

The equilibrium horizontal emittance can be written as Eq. 2.3, where $C_q \approx 3.84 \times 10^{-13}$ m, $J_x = 1 - I_4/I_2 \approx 1$ for separate function magnets, and $I_5 = \int_{dipoles} \frac{H}{\left|\rho^3\right|} ds$. Since the dispersion η function inside the wiggler section is very small, we can assume that there is no emittance contribution from wiggler. $I_5 = \frac{2\pi \langle H \rangle_B}{\rho^2}$, and $\langle H \rangle_B$ is the average of the Courant-Snyder dispersion invariant over the arc bending magnets. We have

$$\gamma \varepsilon_x = \frac{C_q \gamma^3 I_5}{J_x I_2}. \tag{2.3}$$

In Combination with Eqs. 2.1 and 2.2, the required damping time and equilibrium horizontal emittance allow us to determine I_2 and I_5. The arc cell is designed to meet the I_5 requirement, and the wiggler section is designed to provide adequate damping.

Linear Optics

We adopt a TME (Theoretical Minimum Emittance) [2.4] cell lattice for the small damping ring. The phase advance per arc cell is 150°/90° for the horizontal and vertical motion, respectively. Since achieving the target equilibrium horizontal emittance is not a particularly critical issue for a damping ring which is large in comparison with the NLC damping ring and synchrotron light sources, the main considerations driving this choice are chromaticity correction, $\beta_{\max} \leq 49\,\mathrm{m}$ (we assume the magnet pole radius is $r = 5\sigma_{inj} + 5mm = 40mm$), and a larger value of α_p to make the bunch long enough to avoid microwave type instabilities. The maximum beta function is driven by injection beam size and magnet aperture.

The ring is designed with six-fold symmetry and incorporates six long straight sections. Two of the straight sections contain wigglers while the others are filled with FODO cells. They can accommodate RF cavities, tune adjustment sections, and various injection/extraction devices.

For simplicity, our wigglers are similar to those used in the NLC damping ring design. In order to reduce nonlinear perturbations, the average beta function in the wiggler insertion is about 6 m. The small damping ring design incorporates 40 wigglers with a total length of 77 m devoted to wigglers.

The lattice functions for different sections of the ring are shown in Figures 2.2 through 2.7. The main lattice parameters are listed in Table 2.2.

Energy E GeV	5.066
Circumference C m	6113.946
Number of bunches $N_{b,total}$	2820
Number of Trains N_t	60
Number of bunches per train N_b	47
Train to train spacing T_t ns	340
Kicker rise time $\tau_{k,r}$ ns	<6
Kicker fall time $\tau_{k,f}$ ns	<60
Cycle time T_c s	0.2
Injected emittance $\gamma\varepsilon_{x(y)}$ m	0.01
Horizontal extracted emittance $\gamma\varepsilon_x$ m	8×10^{-6}
Vertical extracted emittance $\gamma\varepsilon_y$ m	0.02×10^{-6}
Betatron tune υ_x/υ_y	56.584/41.618
Natural chromaticity ξ_x/ξ_y	-74.6/-55.4
Momentum compaction α_p	0.00014
Maximum beta function $\beta_{x,max}/\beta_{y,max}$ m	49/45
Maximum dispersion $\eta_{x,max}$ m	0.72
Equilibrium horizontal emittance $\gamma\varepsilon_x$ m	5.5×10^{-6}
Equilibrium bunch length σ_z mm	6
Equilibrium momentum spread σ_e	0.0015
RF frequency f_{RF} MHz	494.118
RF harmonic h	10077
RF voltage V_{RF} MV	27.2
Number of particles per bunch N_e	2.0×10^{10}
Current I mA	443
Energy loss per turn U_0 MeV/turn	7.73
Total radiated power P_W MW	3.4
Number of vertical damping time N_τ	7.46
Damping time $\tau_x/\tau_y/\tau_e$ ms	26.8/26.8/13.4

Table 2.2: Principal lattice parameters for the positron damping ring.

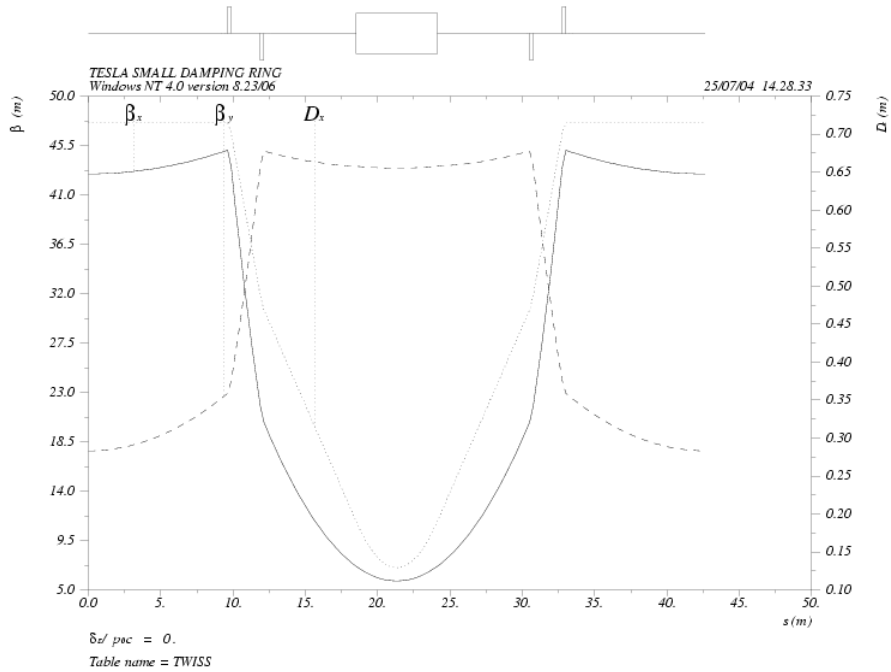

Figure 2.2: Lattice functions in an arc cell.

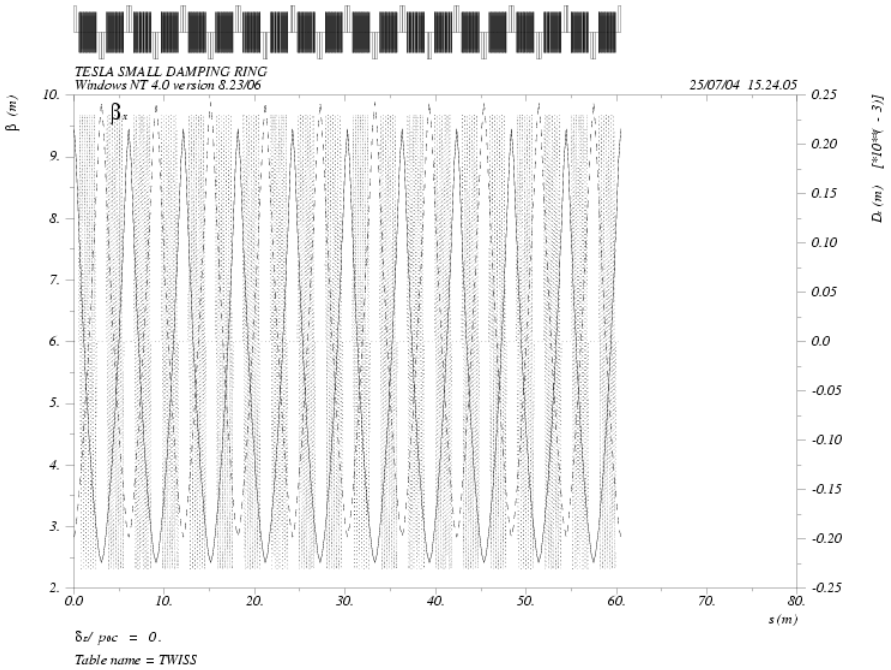

Figure 2.3: Lattice functions for wiggler section

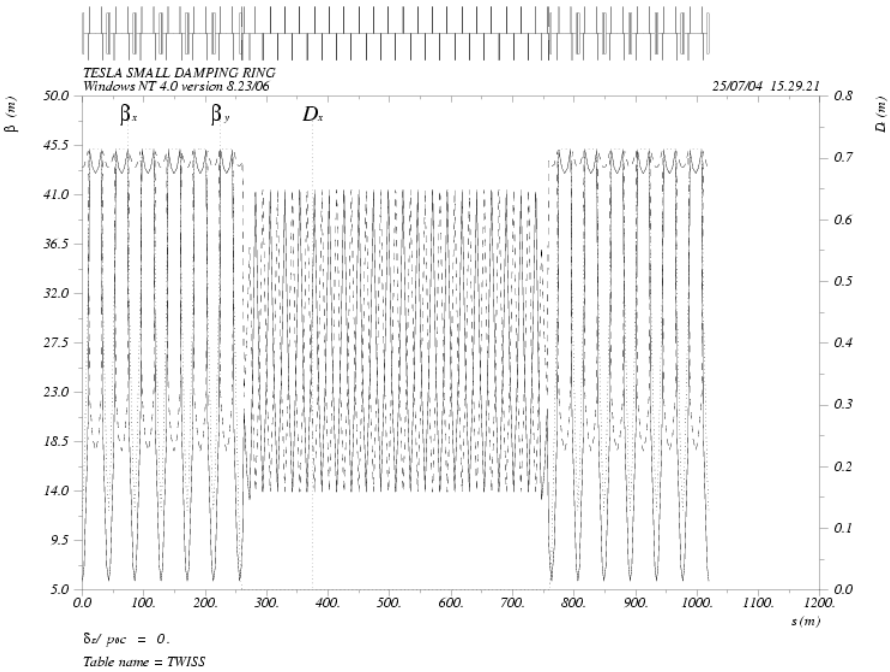

Figure 2.4: Lattice function in a normal sextant

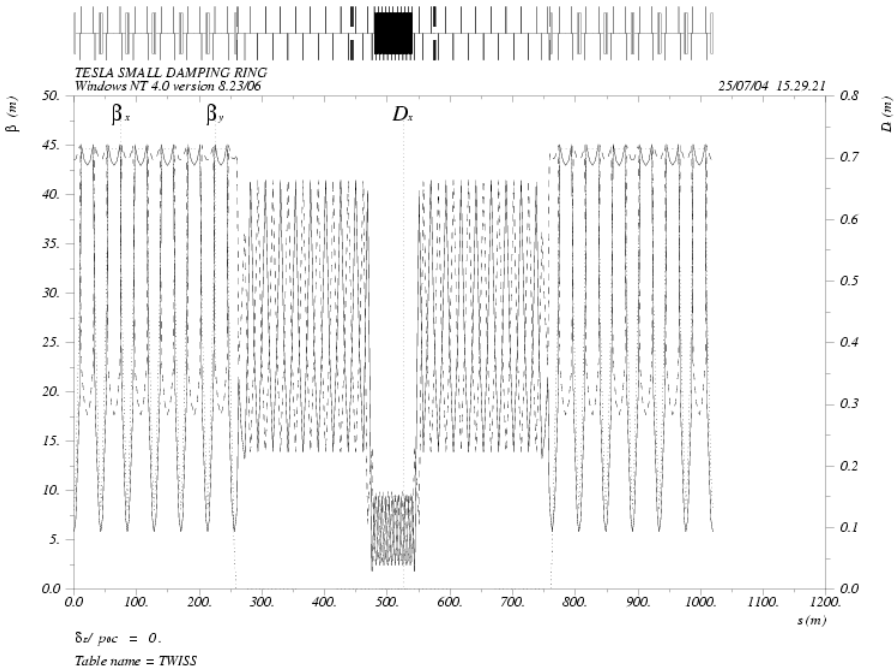

Figure 2.5: Lattice function in a wiggler sextant

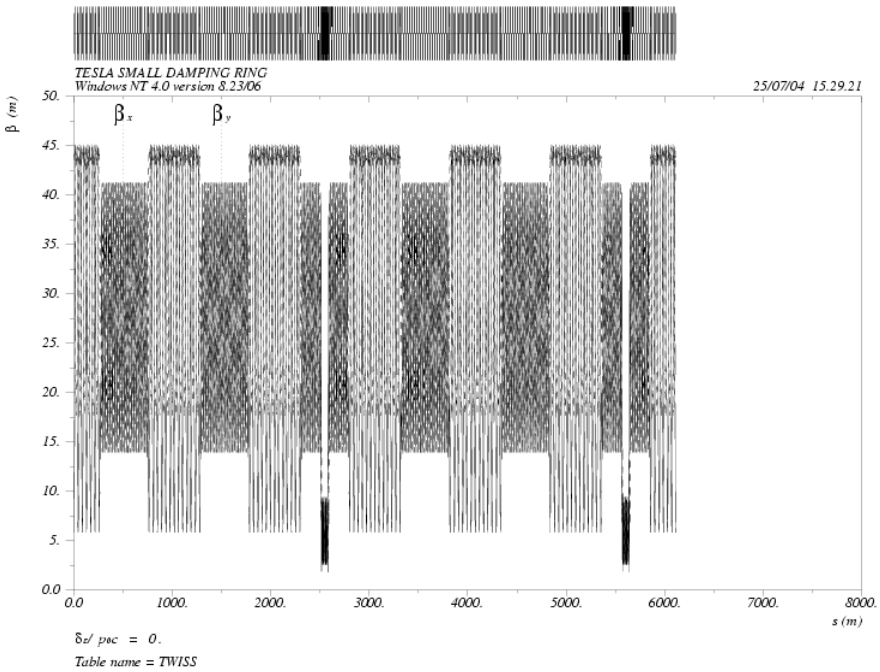

Figure 2.6: Beta functions for the entire ring

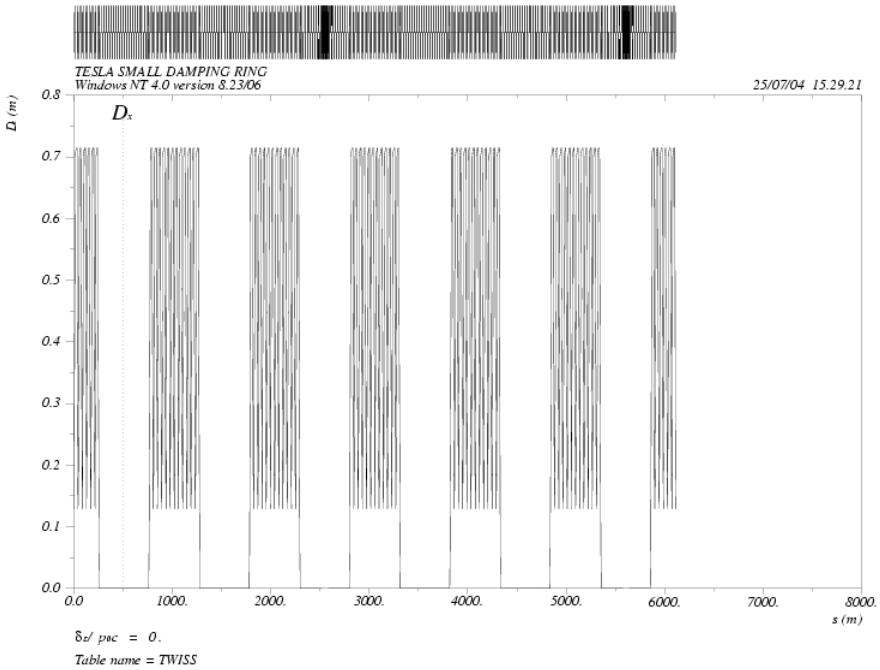

Figure 2.7: Dispersion function for the entire ring

Chromaticity Correction and Dynamic Aperture

As mentioned above, the phase advance per arc cell was chosen to be 150° (90°) for the horizontal (vertical) motion. As a result, the 12 cells per arc cause a net horizontal (vertical) phase advance of 10π (6π) radians. This arrangement helps reduce second order geometric aberrations introduced by the sextupoles. Two sextupole families (SD and SF) are installed in the arc cell in order to eliminate the first-order chromaticity. The resulting variation of tune with momentum spread is ±1% and is shown in Figure 2.8. The working point in tune space is shown in Figure 2.9. The tracked horizontal and vertical phase spaces are shown in Figure 2.10. The dynamic aperture, including linear wiggler effects, is show in Figure 2.11.

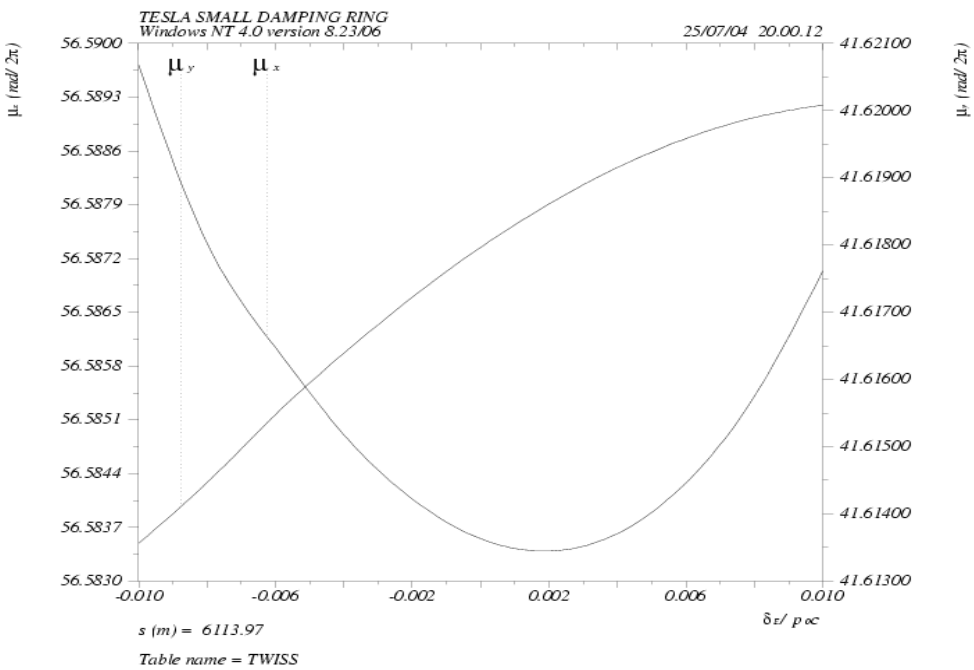

Figure 2.8: Betatron tunes vs. momentum deviation

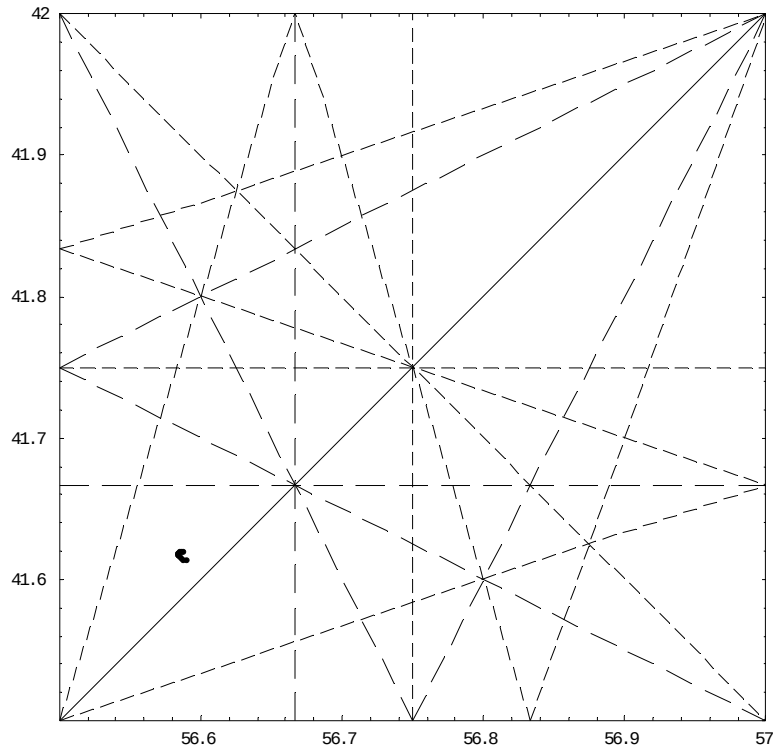

Figure 2.9: Working point in tune space. Resonance lines up to fourth order are shown.

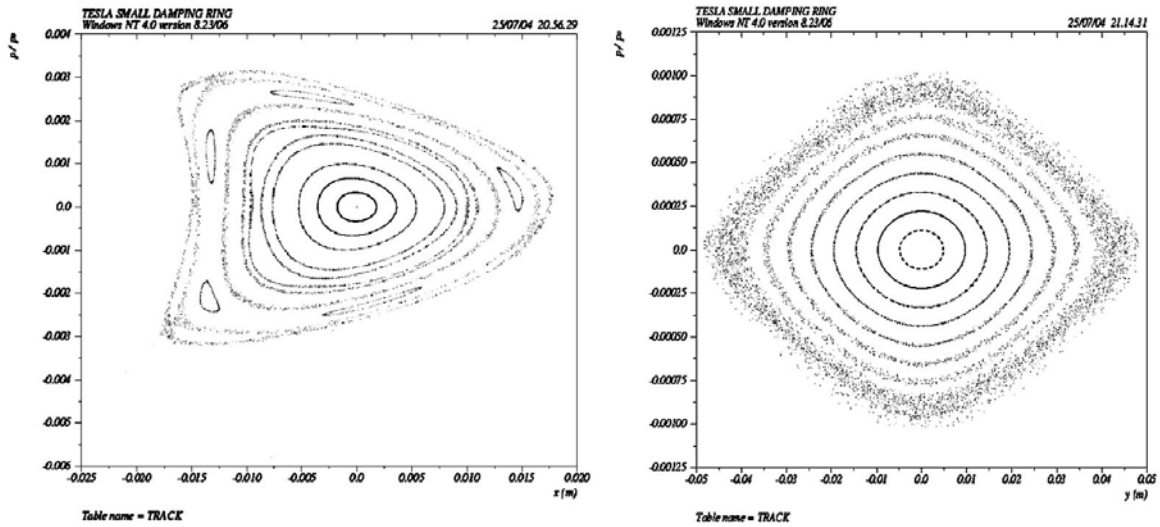

Figure 2.10: Phase space. (a) Horizontal, beta_x = 5.4 m; (b) Vertical, beta_y = 42 m

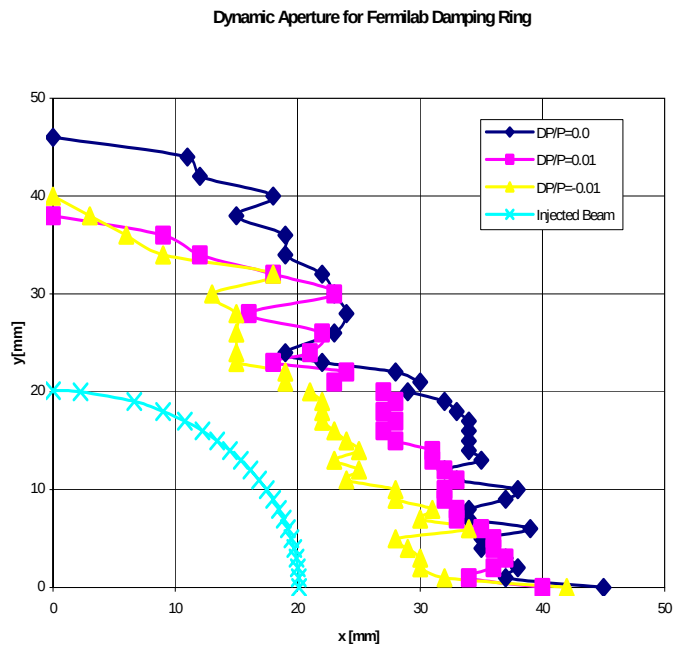

Figure 2.11: Dynamic aperture

Further Work

We will concentrate our future efforts on studies of beam stability issues and the impact of wiggler nonlinearities on particle dynamics. Magnet alignment effects on effective vertical emittance and refinement of beam optics for injection and extraction will also be investigated.

3. Injection and extraction optics

There are two significant aspects of damping ring injection and extraction that deserve mention. Incoming electrons (or positrons) are injected into empty RF buckets in the ring, rather than being added to the contents of bunches already orbiting the ring. In addition, the emittance of an incoming positron bunch is very large. As a result, the injection and extraction optics must be designed to accommodate these beam characteristics while still achieving high injection and extraction efficiencies.

The separation Δx between the orbiting beam and an extracted bunch effected by the kicker is shown in Eq. 3.1:

$$\Delta x = \sqrt{\beta_{kick}\beta_{septum}}\,\sin(\Delta\varphi)\theta_{kick}\,. \tag{3.1}$$

Δx must be large enough to allow installation of a septum and Lambertson magnet in order to further separate the extracted and circulating beams.

The 28 ms damping time is much longer than the 1 ms required to inject the full ILC beam into the damping ring. As a result, the emittance of bunches does not change significantly during the injection cycle so that the injection emittance must be used when calculating the properties of the injection optics associated with separation of injected and circulating beam bunches. Our design specifies acceptances of $5\sigma_{inj}$ for the circulating beam and $3\sigma_{inj}$ for injected beam at the septum, and assumes an additional 4 mm to accommodate the septum itself. As a result, we require

$$\Delta x \geq 8\sigma_{inj} + 4 \text{ mm} = 8\sqrt{\beta_{septum}\varepsilon_{inj}} + 4 \text{ mm} . \tag{3.2}$$

The injection and extraction optics are designed to accommodate either of two different types of kickers that we are studying at Fermilab: a pulsed kicker system with 6 ns rise time (and longer fall time) and a Fourier kicker. Figure 3.1 shows the layout for the injection/extraction optics. Figure 3.2 illustrates profiles for both injected and circulating beam. Table 3.1 lists parameter of the injection/extraction optics..

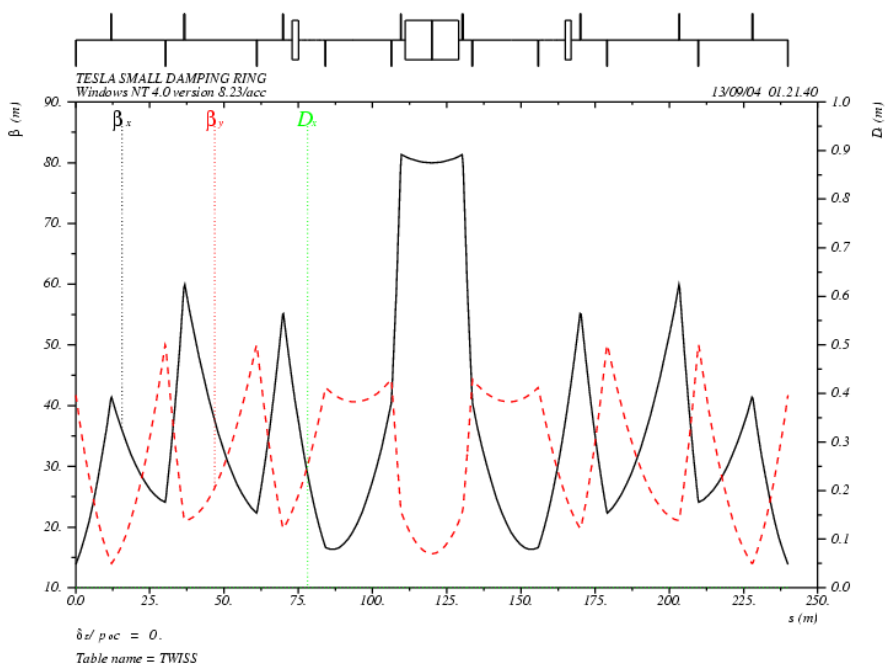

Figure 3.1: Injection and extraction optics ($\beta_{kixk} = 80m$, $\beta_{septum} = 42m$)

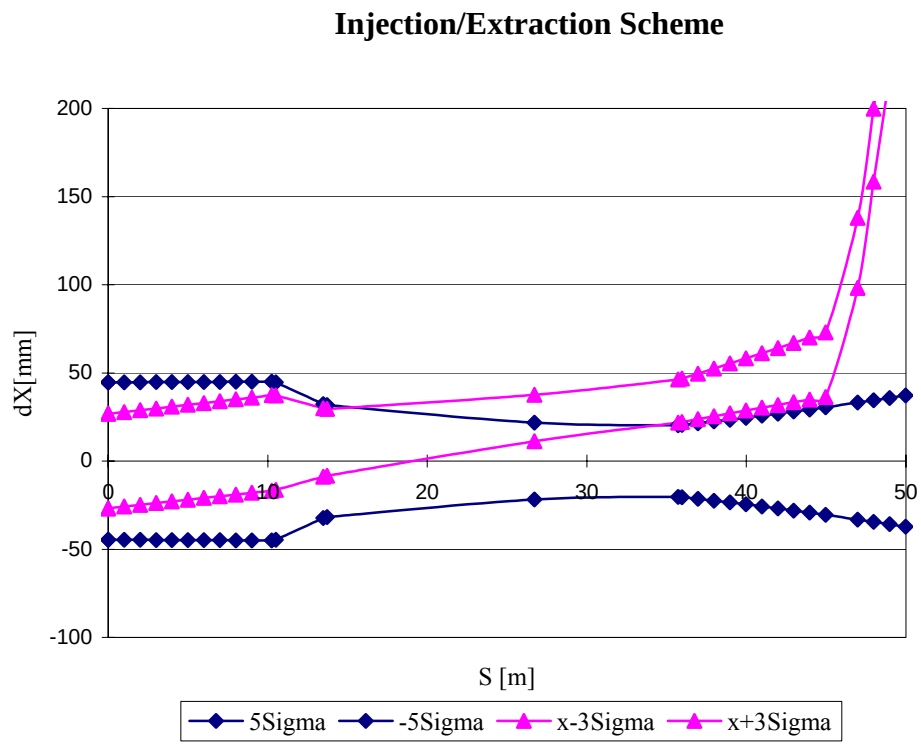

Figure 3.2: Envelopes of injected beam ($3\sigma_{inj}$) and circulated beam ($5\sigma_{inj}$) in the injection region

Name	S [m]	Length [m]	Strength	Beta [m]
Kicker	0	20 (in total)	1mrad	80
QF1	10.25	0.25	0.37[m^-2]	80
QD1	13.47	0.25	0.39[m^-2]	40
QD2	35.72	0.25	0.14[m^-2]	16.9
Septum	44.97	2	0.5[T]	40

Table 3.1: Injection/extraction elements

4. RF and collective effects

RF System

The RF system of the small damping ring is essentially the same as that of the TESLA damping ring. [4.1] It consists of 12 superconducting Niobium 494 MHz cavities having a total shunt impedance $R/Q = 45\ \Omega$ per cell and an unloaded quality factor $Q_0 \approx 10^{10}$ at 2°K. Dissipative material inserted at the inner surface of the beam pipes just outside the cryostat (at room temperature) provides damping for the higher-order modes.

Experience at CESR and KEKB tells us that the quality factor of these higher-order modes can be reduced to a few hundred over the bandwidth 1–3 GHz. These modes will

contribute $Z_0^{\|}/n = 2$ mΩ for the TESLA dog-bone damping ring together with a loss factor of $k_{\|} = 8.8$ V/pC. The TESLA dog-bone damping ring has a circumference of 17 km and bunch length $\sigma_\ell = 6$ mm. For the small damping ring, they scale to $Z_0^{\|}/n = 5.7$ mΩ and $k_{\|} = 8.8$ V/pC. The low frequency inductive impedances $Z_0^{\|}/n$ should be much less because of the large quality factors.

Optimum Coupling Coefficient

For all 12 cavities, the total shunt impedance is $R_s = 5.40 \times 10^{12}\,\Omega$. The total average image current at the RF frequency is twice the average beam current, or $i_{im} = 2en_t n_b N_b c/C = 0.886$ A, since there are $n_t = 60$ trains each containing $n_b = 47$ bunches of intensity $N_b = 2 \times 10^{10}$ particles. With the RF gap voltage $V_{RF} = 27.2$ MV, the power dissipated at the cavity walls is

$$P_c = \frac{V_{RF}^2}{2R_s} = 68.5 \text{ W}. \tag{4.1}$$

The total power delivered to the beam is

$$P_b = \frac{1}{2} i_{im} V_{RF} \sin\phi_s = 3.42 \text{ MW}. \tag{4.2}$$

The synchronous angle is $\phi_s = \pi - 0.284$, determined by $U_0 = 7.273$ MeV (the energy loss per turn), which includes synchrotron radiation, higher-order-mode excitations and parasitic losses. Thus the optimized coupling coefficient of the generator to the cavities is

$$\beta_{op} = 1 + \frac{P_b}{P_c} = 50000. \tag{4.3}$$

The loaded quality factor is therefore $Q_L = Q_0/(1 + \beta_{op}) = 2.00 \times 10^5$ while the loaded shunt impedance is $R_L = R_s/(1 + \beta_{op}) = 108$ MΩ.

Detuning

For the generator current to be in phase with the RF gap voltage, the cavities must be detuned. The detuning angle ψ is determined by

$$\tan\psi = \frac{i_{im} R_L \cos\phi_s}{V_{RF}}, \tag{4.4}$$

yielding $\psi = -1.28$ radians or -73.5°. The detuning is

$$\frac{\omega_r - \omega_{RF}}{\omega_r} = \frac{\tan\psi}{2Q_L} = -8.43 \times 10^{-6}. \tag{4.5}$$

It is possible to detune the cavity frequency downwards by $f_{RF} - f_r = 4.22$ kHz, which is less than one-tenth of the revolution frequency of 49.0 kHz. Because of the high Q_L, the fundamental mode will not drive any longitudinal coupled-bunch instabilities.

Beam Loading

The instantaneous beam loading voltage left inside the cavities after the passage of a bunch is

$$V_{b0} = \frac{eN_b \omega_{RF} R_L}{Q_L} = 5.44 \text{ kV}, \tag{4.6}$$

and is in the direction of i_{im}. When a steady state is reached, the kth bunch in a train sees a beam loading voltage of

$$\tilde{V}_{bk} = \tilde{V}_0 e^{-(k-1)\Delta_L} + \tilde{V}_{b0}\left[\tfrac{1}{2} + e^{-\Delta_L} + \ldots + e^{-(k-1)\Delta_L}\right], \tag{4.7}$$

where $\Delta_L = \delta_L(1 + i \tan \psi)$ is the decay decrement in a bunch spacing, $T_b = 6$ ns, and $\delta = \pi T_b/(Q_L T_{RF})$, with cT_{RF} the RF wavelength. In the above, $\tilde{V}_0 + \frac{1}{2}\tilde{V}_{b0}$ is the beam loading voltage seen by the first bunch in the train due to the excitation by earlier passages of the beam. Since $h_t |\Delta_L| \ll 1$, where $h_t = 56\frac{2}{3}$ is the length of a train including the train gap in bunch spacing,

$$\tilde{V}_0 = i_{im} R_L \cos\psi e^{-i\psi}, \tag{4.8}$$

which has the magnitude $V_0 = 27.2$ MV. Here, we have made the approximation that each of the 60 train gaps is of the same length.

The near equality of V_0 and V_{RF} is not accidental, but is the consequence of the huge optimum coupling coefficient β_{op}, which is a characteristic of superconducting cavities. This near equality shifts the generator voltage in phase with the beam current, thus forfeiting all possible Robinson's phase stability. As a result, the alleviation of any jitter or offset of bunches from the synchronous phase has to rely solely on radiation damping. If a shorter damping time (<13.5 ms) is desired, a fast RF feedback and phase loop must be installed.

The difference in beam loading voltage experienced by the last and first bunches in the train can now be computed as

$$\Delta\tilde{V}_b = \frac{(n_b - 1)(h_t - n_b)}{h_t} V_{b0} = 427 \text{ kV}, \tag{4.9}$$

which becomes independent of the complex decay decrement Δ_L, where the assumption $h_t|\Delta_L| \ll 1$ has been made. Notice that this difference phasor is in the direction of i_{im} and will perturb the RF gap voltage experienced by the last bunch. The synchronous angle (in radians) experienced by the last bunch is also shifted by

$$\Delta\phi_s = \frac{\Delta V_b \cos\phi_s}{V_{RF}} = 0.0015. \tag{4.10}$$

This variation in synchronous angle $\Delta(\pi - \phi_s) = -0.086°$ in the last bunch. This variation is small and, if not corrected, will lead to an increase in half bunch length by only $|\Delta\phi_s|/\omega_{RF} = 0.47$ ps.

Impedance of the Vacuum Chamber

Space Charge

The designed normalized rms beam emittance is ε_{xN} (ε_{yN}) = 8.00×10^{-6} (2.00×10^{-8}) πm with betatron tune ν_x (ν_y) = 56.584 (41.618). The mean betatron function is therefore $\bar{\beta}_x$ $(\bar{\beta}_y) = 17.20$ (23.38) m. The rms vertical beam radius is $\sigma_y = \sqrt{\bar{\beta}_y \varepsilon_{yN}/\gamma} = 6.87$ μm, where $E = \gamma mc^2$ is the electron energy, m its rest mass, and c the velocity of light. The horizontal rms dispersion function is η_{rms} =0.311 m and the rms energy spread $\sigma_E = 0.00150$.

Since the dispersion function of the lattice and energy offset of a particle in the beam are statistically independent, the rms horizontal beam radius is therefore

$$\sigma_x = \sqrt{\bar{\beta}_x \varepsilon_{xN}/\gamma + (\eta_{rms}\sigma_E)^2} = 482\ \mu\text{m}. \tag{4.10a}$$

Notice that the horizontal emittance contributes only 118 μm to the beam size whereas the dispersion contributes 467 μm. Thus the average horizontal beam size is dominated by dispersion. The TESLA dog-bone ring, on the other hand, is quite different. The arcs are of length 1.9 km, only about 11% of the whole ring. As a result, the rms dispersion should be about 0.03 m, an order of magnitude smaller than that of the small damping ring design. In addition the rms horizontal beam radius coming from the emittance is 174.9 μm because the betatron function is twice as big as the small ring design. The horizontal beam size is therefore dominated by emittance. This difference has an important bearing on the incoherent space-charge tune shift to be discussed below.

Incoherent Self-Field Tune Shift

The incoherent space-charge tune shift at the center of the beam is, for the vertical,

$$\Delta\nu_y = -\frac{N_b r_e R}{2\pi\gamma^3\sigma_y\left(\sigma_x+\sigma_y\right)\nu_y B} = -0.0261 \tag{4.11}$$

and $\Delta\nu_x = -0.00027$ for the horizontal, where $r_e = 2.8179 \times 10^{-15}$ m is the classical electron radius and $N_b = 2 \times 10^{10}$ is the number of particles per bunch. The bunching factor $B = \sqrt{2\pi}\sigma_z / C = 2.46\times10^{-6}$, has been used. Notice that Eq. (4.11) gives the maximum vertical space-charge tune shift for particles at the center of the bunch. The vertical space-charge tune shift averaged over all particles in the bunch will be much less.

Simulations of the TESLA dog-bone damping ring reveal that a maximum space-charge tune shift of −0.1 is tolerable. [4.2] The maximum vertical space-charge tune shift of the TESLA dog-bone damping ring is $\Delta\nu_y = -0.31$. (The TESLA Report gives $\Delta\nu_y = -0.23$ because it has been incorrectly assumed that the average betatron functions are the same horizontally and vertically.)

There are two reasons why this tune shift is an order of magnitude larger than that of the small ring design. First, since the vertical betatron tune of the TESLA ring is $\nu_y = 44.18$, almost the same as the small ring design, the space-charge tune shift is essentially proportional to the square of circumference of the ring and the TESLA dog-bone is 2.78 times larger. Second, the horizontal beam size of the small ring has been enlarged by a factor of 3 because of the dispersion, but this enlargement is almost negligible in the TESLA ring. In the analysis of Decking and Brinkmann, [4.2] the maximum vertical space-charge tune shift can be reduced to $\Delta\nu_y = -0.035$ by initiating horizontal and vertical coupling at the long straight sections so that average vertical and horizontal emittances are equal to about one half the designed ε_{xN}. No such coupling will be necessary for the small damping ring.

Space-Charge Impedances

Taking the vertical radius of the beam pipe as $b = 1$ cm, space-charge impedances experienced by the beam are

$$\begin{aligned} \frac{Z_0^{\parallel}}{n} &= i\frac{Z_0}{2\gamma^2}\left(\gamma_e + 2\ln\frac{b}{\sqrt{2}\sigma_y}\right) = i0.028\ \text{m}\Omega \\ Z_1^{\perp} &= i\frac{Z_0 R}{\gamma^2}\left(\frac{1}{\sigma_y\left(\sigma_y+\sigma_x\right)} - \frac{1}{b^2}\right) = i1.11\ \text{M}\Omega/\text{m}, \end{aligned} \tag{4.12}$$

where $\gamma_e = 0.57722$ is Euler's constant. We see that the longitudinal space-charge impedance is small and will be within the microwave stability limit. The vertical space-charge impedance, on the other hand, is large and is larger in magnitude than the transverse wall-resistive impedance at the $(1 - Q)$ line. However, it may help to increase the threshold of transverse mode-mixing instability of the beam as discussed below. [4.3] The space-charge impedances of the TESLA design are comparable.

Wall impedance

The beam pipe is made of aluminum with resistivity $\rho_s = 2.65 \times 10^{-8}$ Ω-m. The skin depth at the revolution frequency is therefore $\delta_{s0} = \sqrt{2\rho_s/\omega_0\mu} = 0.370$ mm. Assuming a round beam pipe of radius $b = 1$ cm, the longitudinal and transverse impedances are

$$\begin{aligned} Z_0^{\parallel} &= (1-i)\frac{\rho_s R}{\delta_{s0} b}\sqrt{n} = (1-i)6.97 n^{1/2}\ \Omega, \\ Z_1^{\perp} &= \frac{2c}{b^2}\frac{Z_0^{\parallel}}{\omega} = (1-i)135.6\left|n-\nu_{x,y}\right|^{-1/2}\ \mathrm{M\Omega/m}. \end{aligned} \tag{4.13}$$

The loss factor $k_{\parallel}$ is the energy loss of the bunch if the total charge inside the bunch is one Coulomb. It can be written as

$$k_{\parallel} = \frac{1}{2\pi}\int_{-\infty}^{\infty} Z_0^{\parallel}(\omega)\, h(\omega)\, d\omega, \tag{4.14}$$

where $h(\omega) = e^{-\omega^2\sigma_\tau^2}$ (with σ_τ the rms bunch length) is the power spectrum of the bunch. For the resistive wall, we get

$$k_{\parallel} = \frac{\Gamma\left(\frac{3}{4}\right)}{2\pi\omega_0^{1/2}\sigma_\tau^{3/2}}\mathrm{Re}\, Z_0^{\parallel}\Big|_{n=0} = 27.4\ \mathrm{V/pC}. \tag{4.15}$$

Button BPM

We follow the BPM computation presented in the NLC ZDR. [4.4] For a set of four buttons, the magnitude of the longitudinal impedance as calculated using MAFIA, consists of a first resonance of 14 Ω at 9.1 GHz with Q ~300, and a second resonance of 16 Ω at 12 GHz with Q ~50.

The revolution frequency of the small damping ring is f_0=49.0 kHz. Thus these two resonances give $\mathrm{Re}\, Z_0^{\parallel}/n = 0.0754$ mΩ and 0.0653 mΩ at the respective resonant frequencies.

For a high Q resonance,

$$\frac{\mathrm{Re}\, Z_0^{\parallel}}{n} = \begin{cases} \dfrac{R_s}{n_r} \\ \dfrac{nR_s}{n_r^2 Q^2} \end{cases} \qquad \frac{\mathrm{Im}\, Z_0^{\parallel}}{n} = \begin{cases} \dfrac{1}{2}\dfrac{R_s}{n_r} & \omega \sim \omega_r \\ \dfrac{1}{Q}\dfrac{R_s}{n_r} & \omega \ll \omega_r \end{cases} \tag{4.16}$$

where $n_r = \omega_r/\omega_0$, ω_r is the resonant frequency, and R_s is the shunt impedance. At low frequencies, the reactive impedance for a set of 4 buttons is $\mathrm{Im}\, Z_0^{\parallel}/n = 0.00156$ mΩ (0.00025 mΩ from the first resonance and 0.00131 mΩ from the second). On the other hand, $\mathrm{Im}\, Z_0^{\parallel}/n = 0.0377$ mΩ and 0.0327 mΩ near the first two resonances.

There are 594 quadrupoles in this ring. If a set of BPMs is installed at the end of each quadrupole, these 594 BPMs contribute $\mathrm{Re}\, Z_0^{\parallel}/n = 44.8$ mΩ (38.8 mΩ) near the resonance at 9.1 GHz (12.0 GHz). $\mathrm{Im}\, Z_0^{\parallel}/n$ will be half of those near the resonances and 0.93 mΩ at low frequencies.

The MAFIA calculation for energy loss gives $k_{\parallel} = 0.0203$ V/pC for each BPM set. But the NLC damping ring electron bunch length is $\sigma_\ell = 3.3$ mm while the small damping ring electron bunch length is $\sigma_\ell = 5.67$ mm. Assuming a $\sigma_\ell^{-1/2}$ dependence the loss factor for all the BPMs in the small ring will be 9.20 V/pC.

Impedance summary

The TESLA Design Report assigns 17 mΩ to the non-inductive part of $Z_0^{\parallel}/n$ for kickers and 11 mΩ to the inductive part of $Z_0^{\parallel}/n$ for bellows and another 5 mΩ to the inductive part of $Z_0^{\parallel}/n$ for "other components." We scale[3] them according to the size of the ring and obtain 48 mΩ for kickers, 11 mΩ for bellows, and 5 mΩ for others. Table 4.1 presents a summary of these quantities.

	$Z_0^{\parallel}/n$ (mΩ)	$k_{\parallel}$ (V/pC)
Noninductive		
RF cavities	5.7	8.8
Resistive wall ($n = 0$)	7.0	27.4
BPMs	44.8	9.2
Kickers	~48	~40
Total	~105	
Inductive		
Bellows	~11	~1.3
BPMs	44.8	
Others	~5	~0.6
Total	~60.8	
Total loss factor		~87.63

Table 4.1: Longitudinal impedance per harmonic and loss factor for the small damping ring from various contributions.

[3] The number of bellows increases as the ring size and we assume the same for "other components".

Single Bunch Instabilities

Microwave Instability

For a short bunch, the mixing of azimuthal modes 1 and 2 causes longitudinal instability. The stability limit is given by

$$\left.\frac{Z_0^{\parallel}}{n}\right|_{eff} = \frac{2\pi\alpha_p E}{eI_{pk}}\left(\frac{\sigma_E}{E}\right)^2 \tag{4.17}$$

where α_p is the momentum compaction factor, I_{pk} is the peak current, and $\left.Z_0^{\parallel}/n\right|_{eff}$ is the impedance weighted by the power spectrum $h(\omega)$ of the bunch mode under consideration. For a damping ring, this instability must be avoided. If not, the bunch length will grow when the bunch becomes unstable. When saturated, the instability stops and the bunch length will be shortened by radiation damping to a value that the instability starts again. When this "saw-tooth" oscillation of bunch length took place in the SLAC SLC damping rings, the bunch would be incorrectly launched into the linac and might eventually be lost on the downstream collimators, causing the linac to trip the machine protection circuits.

For the small damping ring, this stability limit is $\left.Z_0^{\parallel}/n\right|_{eff}$ =150 mΩ. The rms bunch length is $\sigma_\tau = \sigma_\ell/c$ = 20.0 ps and total bunch length is assumed to be $\tau_L = 4\sigma_\tau$ = 80.0ps. The power spectra of the azimuthal modes 1 and 2 peak at $f_1 \sim 2/(2\tau_L)$ = 12.5 GHz and $f_2 \sim 3/(2\tau_L)$ = 18.8 GHz, with half-widths ~6.3 GHz. They are well above the beam pipe cutoff frequency f_c ~11.4 GHz (assuming beam pipe radius b = 1 cm), where the coupling impedance starts rolling off. Apparently, we do not have enough impedance to drive this instability.

For the TESLA damping ring, the stability criterion of Eq. 4.17 gives a comparable stability limit. Since the momentum compaction and fractional energy spread are slightly smaller, ($\alpha_p = 1.20\times10^{-4}$ versus 1.41×10^{-4}, $\sigma_E/E = 1.30\times10^{-3}$ versus 1.50×10^{-3}), the TESLA stability limit becomes $\left.Z_0^{\parallel}/n\right|_{eff}$ =100 mΩ. As for the NLC damping ring, based on ZDR data (α_p = 0.000465; σ_E/E = 0.00090; σ_ℓ = 3.9 mm; E = 1.98 GeV; $N = 1.57\times10^{10}$ per bunch) the stability limit is $\left.Z_0^{\parallel}/n\right|_{eff}$ =61 mΩ.

Transverse Mode-Coupling Instability

Transverse mode-coupling instability (TMCI), sometimes known as the strong head-tail instability, is one of the cleanest instabilities observed in an electron storage ring. The rigid dipole mode, also known as the azimuthal m = 0 mode, shifts downwards with beam intensity, a behavior generally associated with short bunches. In contrast, the azimuthal

m = -1 mode is not much affected. When the beam intensity is high enough, the m = 0 mode meets the m = -1 mode and an instability occurs. The threshold is roughly given by shifting the m = 0 mode by the synchrotron frequency, and can be represented this way:

$$Z_1^{\perp}\Big|_{eff} \approx \frac{2E\nu_y\nu_s\omega_0^2\tau_L}{eI_b c}, \tag{4.18}$$

where $Z_1^{\perp}\Big|_{eff}$ is the transverse impedance weighted over the longitudinal power spectrum $h(\omega)$ of the bunch mode under consideration. With total bunch length $\tau_L = 4\sigma_\ell/c$, we obtain the stability limit of $Z_1^{\perp}\Big|_{eff}$ = 2.34 MΩ/m.

Since the mixing is between the modes m = 0 and m = -1, the frequency of the driving force should be of lower frequency than that driving the longitudinal mode-mixing instability, in the range from 6.3 to 12.5 GHz. Unfortunately, an estimation of the broadband transverse impedance has not been made for the ring. If we employ the Panofsky-Wenzel-like relation

$$Z_1^{\perp} = \frac{2c}{b^2}\frac{Z_0^{\parallel}}{\omega}, \tag{4.19}$$

we obtain the longitudinal-equivalent limit of $Z_0^{\parallel}/n\Big|_{eff}$ =120 mΩ. From the estimate made in Table 4.1, this threshold may be of concern in this analysis.

For the small damping ring, the space-charge contribution to the transverse impedance is of the order of the TMCI threshold. In addition, the incoherent space charge tune shift is large and is of the same order of magnitude as the synchrotron tune. Under these circumstances, the threshold criterion of Eq. 4.18 may not be valid. This is because non-space charge transverse impedance shifts the m = 0 mode downward without much effect on the other modes. Instability occurs when the m = 0 mode meets the m = -1 mode. On the other hand, the transverse space-charge impedance shifts all modes downward except the m = 0 mode. Thus if the transverse space charge impedance is large enough, it will be much more difficult for the m = 0 and m = -1 modes to meet. In other words, the threshold of the transverse mode-coupling instability will be pushed to a much higher current in the presence of strong space charge. Thus it requires further detailed study with space charge included to determine whether the present design will be subjected to TMCI or not.

For the TESLA dog-bone damping ring, the synchrotron tune ν_s scales like $R^{1/2}$ while the betatron tune is ν_y = 44.2, very close to the 45.1 of the small ring, where R is the mean radius of the ring. Equation 4.18 suggests that the stability limit for the TESLA dog-bone damping ring scales with $R^{-1/2}$ or 1.80 MΩ/m. With the Panofsky-Wenzel-like relation, this translates to $Z_0^{\parallel}/n$=133 mΩ, large compared to the estimate of the inductive and non-inductive impedances of $|Z_0/n| \approx$ 29 mΩ and 25 mΩ respectively for the vacuum chamber of the TESLA dog-bone ring. Again, the large incoherent space-charge tune shift should help raise the threshold current to a higher value, even after the reduction

associated with horizontal-vertical coupling,. The transverse mode-coupling instability limit for the NLC damping ring is $Z_1^{\perp}\big|_{\text{eff}}$ ~0.50 MΩ/m.

Multi-Bunch Instabilities

Longitudinal Coupled-Bunch Instabilities

Each RF cavity has a shunt impedance of R/Q = 45 Ω. We assume the same value for higher-order modes, which will be damped by dissipative material to Q ~100. Thus for all 12 cavities the largest possible shunt impedance for the higher-order modes will be R_s = 54 kΩ.

The frequency at which the bunch spectrum rolls off is $\omega_r/(2\pi) = 1/(2\tau_L) \approx c\big/\left(4\sqrt{6}\sigma_z\right)$, approximately 5.1GHz. Assuming that the shunt impedance falls on a synchrotron sideband at roughly this frequency, the fastest longitudinal coupled-bunch growth rate is given by

$$\frac{1}{\tau} = \frac{e\alpha_p n_t n_b I_b R_s \omega_r}{4\pi E \nu_s}. \tag{4.20}$$

In Eq. 4.20 I_b is the average bunch current and $n_t n_b$ = 2820 is the total number of bunches. Since the value of $1/\tau$ is only 49.5 s^{-1}, the shortest growth time is 20.1 ms.

The above discussion assumes a ring filled with equally spaced *pointlike* bunches of equal intensity. The finite length of the bunch will introduce a damping factor roughly equal to $\exp\left(-\omega_r^2\sigma_\tau^2\right)$, which is 0.66 for the situation above. The concentration of bunches at 60 locations will further lower the growth rate. In short, the shortest growth time may be longer than the radiation damping time of 13.5 ms. Thus, no longitudinal coupled-bunch instability will materialize, and a broadband multibunch feedback system may not be necessary.

For the TESLA dog-bone ring, the shortest growth time is much longer. The average bunch current I_b scales with R^{-1} while the synchrotron tune ν_s scales with $R^{-1/2}$, so the shortest growth time scales with $R^{-3/2}$, or 4.6 times longer. In addition, the momentum compaction $\alpha_p = 1.2\times10^{-4}$ is smaller than in the small ring design and the rms bunch length $\sigma_\ell = 6$ mm is slightly longer. All these factors bring the shortest growth time for pointlike bunches to 134 ms, about 4.7 damping times.

Transverse Coupled-Bunch Instabilities

The transverse resistive wall impedance will drive transverse coupled-bunch instabilities. The fastest growing mode is driven by the vertical ($n - Q$) betatron line. The growth rate is

$$\frac{1}{\tau} = \frac{e n_b I_b c}{4\pi \nu_y E} \operatorname{Re} Z_1^{\perp} F', \tag{4.21}$$

where F′ ~ 0.8 is a form factor which depends on the longitudinal linear distribution. Although the betatron tune is $\nu_y = 41.6$, let us assume a residual tune of (42 – Q) = 0.5 since $n = 42$. The transverse wall impedance at the $(42 - Q)$ line is $\mathrm{Re}\, Z_1^{\perp} = 192$ MΩ/m and the growth rate is 9620 s^{-1} (growth time 0.10 ms or 5 turns).

We can compare this growth rate with the TESLA dog-bone damping ring. The longitudinal resistive-wall impedance $Z_0^{\parallel}$ scales with $R^{1/2}$ because the skin depth at revolution harmonic scales with $R^{1/2}$. Thus the transverse resistive-wall impedance $Z_1^{\perp}$ scales with $R^{3/2}$ because it is proportional to $Z_0^{\parallel}/n$. The average bunch current will be smaller and scales with R^{-1}. Thus $I_b\, \mathrm{Re}\, Z_1^{\perp}$ (and therefore the growth rate) scales with $R^{1/2}$ since the vertical betatron tune of the TESLA ring is 44.18, very close to that of the small ring design. Thus the transverse coupled-bunch instability growth rate of the TESLA dog-bone ring will be $\tau^{-1} = 1910\ s^{-1}$.

Due to the short bunch length, a shift towards positive chromaticity does not help at all. This is because it requires a chromaticity $\xi_y \approx \alpha_p/(2f_0\tau_L) = 144$ to shift the mode spectrum of the bunch by $\Delta\omega = \pi/\tau_L$. Coating the beam pipe with a thin layer of copper, however, will further lower the growth rate. A tune spread supplied by octupoles can also provide some Landau damping.

The remaining instability must be alleviated with a low-bandwidth feedback mode damper. Although the damping has to be accomplished in 5 turns, the damper power required should be rather weak, because the rigidity of the beam at 5.066 GeV is quite low (compared to the Fermilab Main Injector 150 GeV beam). On the other hand, a damping ring (whose main purpose is to produce bunches with very low transverse emittances) is quite different from a proton storage ring. We should not be satisfied with just the control of transverse instabilities. We must make sure that the transverse jitter of bunches remains small enough so that the required emittances can be achieved at extraction. For this reason, the sensitivity of the pickups and the specification of the damping kickers must be studied carefully, and further investigation is necessary.

Electron Clouds and Trapped Ions

Electron-Cloud Effect

Electrons will be generated in the vacuum chamber of the damping ring due to residual gas ionization and secondary emission of residual gas ions or molecules hitting the walls of the vacuum chamber. In the positron ring, the electron cloud will interact with the positron beam leading to a growth in transverse emittance. This interaction is short-range and the driving force can be represented by a short-range transverse wake W_1 left one bunch spacing ahead. [4.5] This wake, computed for PEP-II, gives $W_1 \lesssim 1\times10^5\ m^{-2}$ in cgs units (890×10^{12} V/Coul/m in mks units). The amplitude of transverse oscillation has a growth rate of

$$\frac{1}{\tau} \approx \frac{eI_b R W_1}{\nu_y E}, \tag{4.22}$$

or 301 s^{-1}, corresponding to a growth time of 3.33 ms.

The electron cloud can be greatly reduced by wrapping the beam pipe with solenoids. For example, simulation of the HER of KEKB shows that the transverse wake coming from the electron cloud is $W_1 \lesssim 300\ \mathrm{m}^{-2}$, [4.6] which brings the growth rate to 1.11 s^{-1}. This is unimportant since the whole beam storage time is only about 0.2 s. For the TESLA dog-bone ring, this growth rate will be of comparable size because $I_b R$ does not depend on the size of the ring and also because the vertical betatron tune is comparable to that of the small ring design.

Trapped Ions

Ions are generated in the vacuum chamber from residual gas; the electron beam traps positively charged ions. In the potential well of the electron beam, the trapped ions perform transverse oscillations with the ion-bounce angular frequencies

$$\omega_{ix,y} = \sqrt{\frac{3N_b r_p c}{\sigma_{x,y}\left(\sigma_x + \sigma_y\right) A T_b}}, \tag{4.23}$$

where $r_p = 1.5347\times10^{-18}$ m is the classical proton radius, A is the molecular weight of the ion, and T_b is the bunch separation. Eq. 4.23 is obtained by averaging the individual kicks transferred to the ion from the pointlike electron bunches over the whole train. The ions will be cleared at the bunch gaps if $\omega_{ix,y} T_b > 2$, otherwise they will remain trapped.

For CO^+ with $A = 28$, the ion-bounce angular frequencies are ω_{ix} =21.6 MHz and ω_{iy} = 181 MHz. The conditions for trapped CO^+ and H_2^+ at a pressure of 10^{-10} Torr are listed in Table 4.2, both for the small ring and the TESLA dog bone. The results show that H_2^+ will not be trapped vertically in the small ring design and only CO^+ will be trapped horizontally in the dog-bone design.

	Small ring	Dog bone
Bunch spacing T_b (ns)	6	20
H_2^+		
Test for trapping: $\omega_{ix}T_b$	0.49	2.37
$\omega_{iy}T_b$	4.06	9.40
CO^+		
Test for trapping: $\omega_{ix}T_b$	0.13	0.64
$\omega_{iy}T_b$	1.08	2.51
Linear Theory for CO^+		
Fast-ion growth time: τ_x (ms)	1020	1330
τ_y (ms)	1.28	2

Table 4.2: Possible fast-ion instabilities for trapped ions in the small damping ring and TESLA dog-bone ring at the vacuum pressure for 10^{-10} Torr.

While ions oscillate inside the electron beam, electrons also oscillate inside the ion "beam." In the absence of external transverse focusing, the small-amplitude electron-in-ion bounce angular frequency is

$$\omega_{ex,y} = \sqrt{\frac{4\lambda_i r_e c^2}{\gamma\sigma_{x,y}\left(\sigma_x + \sigma_y\right)}}, \tag{4.24}$$

where λ_i is the ion linear density. Compared with the ion-bounce frequency in Eq. (4.23), there is an extra factor of γ in the denominator because the electrons are orbiting the ring. The extra factor of 2 in the numerator appears because ions are at rest when generated by the electrons, implying that the transverse radii of the ion "beam" are a factor of $\sqrt{2}$ smaller.

The growth time in the linear theory can be expressed as

$$\tau_{x,y} = \frac{2\omega_{x,y}}{\omega_{ex,y}^2 \omega_{ix,y} \tau_{tr}}, \tag{4.25}$$

where τ_{tr} is the length of the bunch train. Plugging in numbers gives τ_x (τ_y) = 1020 (1.28) ms. Thus there is no problem in the horizontal direction, but some feedback device is necessary for the vertical. However, it is unclear why the growth times for the TESLA dog-bone are so much shorter than those for the small damping ring even though the trapping test shows that CO^+ will not be (vertically) trapped in the former. It is also unclear why the horizontal growth times are so much larger than the vertical ones, in spite of the fact that the trapping test shows that trapping will be less severe in the horizontal. In fact, the expression of the growth time in Eq. 4.25 assumes a uniform electron beam of the length of the whole train, without gaps, so that ions are trapped inside.

In order to study the problem more realistically, a number of simulations have been performed. To save time on computation, only the first 1000 turns were simulated (note that total storage requires ~10,000 turns). The vacuum pressure was increased to 10^{-8} to enhance the growth. All bunches were considered as pointlike with a transverse offset selected randomly up to 1/100 of 6.6×10^{-6} m, roughly the vertical rms beam radius.

The vertical oscillation amplitudes for the first 1000 turns are shown in Figs. 4.1a and 4.1b for bunches 20 and 47 in a train (as picked up by a BPM). We see in the figures that the growths in amplitude are very rapid, reaching $\pm8\times10^{-8}$ m for bunch 20 and $\pm2.5\times10^{-4}$ m for bunch 47 in 1000 turns, and appear to continue, although the initial beam displacement was random between $\pm6.6\times10^{-8}$ m.

A feedback with a gain of 0.2 was then applied and the simulation repeated. We see that with feedback the amplitudes have been controlled to within $\pm150\times10^{-6}$ for bunch 20 and $\pm25\times10^{-6}$ m for bunch 47. However, the oscillation amplitude for bunch 20 is still very much larger than the rms bunch radius. It is unclear why the growth of the last bunch of the train has been much less rapid than the 20th. The theory of fast beam-ion instability and some simulations [4.7] suggest that the instability growth rate increases with the square of the bunch position. On the other hand, we find in this train of 47 bunches that bunches in the center of the train have much larger growths than the head and the tail bunches.

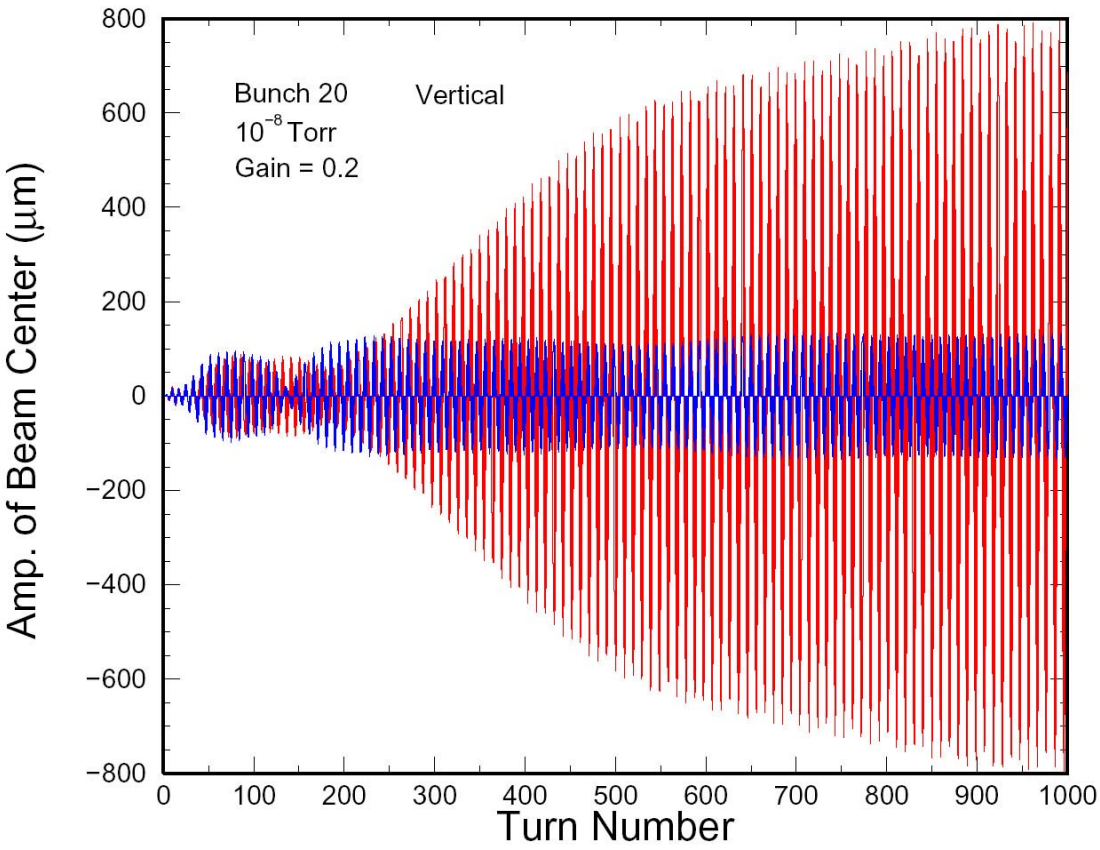

Figure 4.1a: (color) Vertical amplitudes of the 20th bunch in the train for the first 1000 turns at vacuum pressure 10^{-8} Torr without and with feedback of gain 0.2. The growths had been very fast, but were controlled by the feedback.

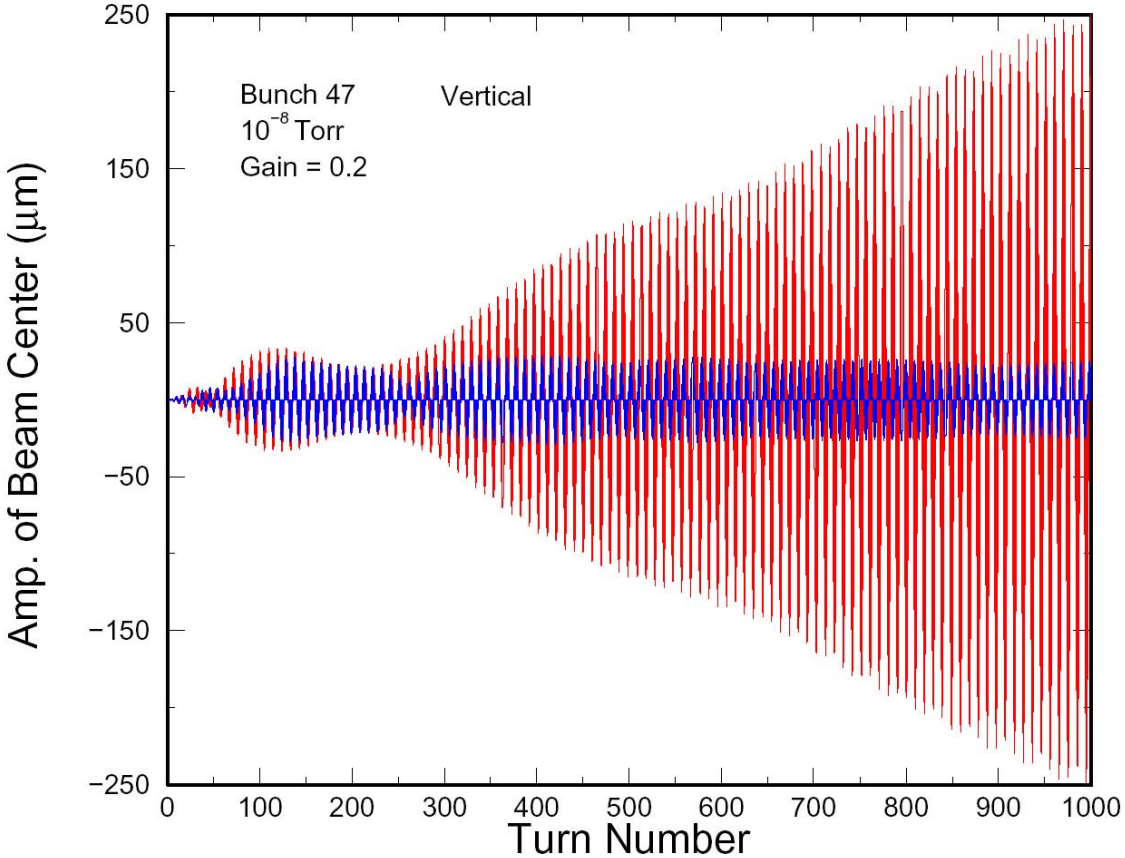

Figure 4.1b: (color) Vertical amplitudes of the 47th bunch in the train for the first 1000 turns at vacuum pressure 10^{-8} Torr without and with feedback of gain 0.2. The growths had been very fast, but were controlled by the feedback.

We repeat the simulations with vacuum pressure at 1×10^{-10} Torr. The results for bunches 20 and 47 are shown in Figs. 4.2a and 4.2b. Now the growth is much less in the first 1000 turns and goes up to $\pm15\times10^{-6}$ m for bunch 20 and $\pm2.3\times10^{-6}$ m for bunch 47. Feedback at a gain of 0.20 stabilizes the growth to within $\pm1.5\times10^{-6}$ m for bunch 20 and $\pm0.4\times10^{-6}$ m for bunch 47, which are within one sigma of the vertical half size of the beam.

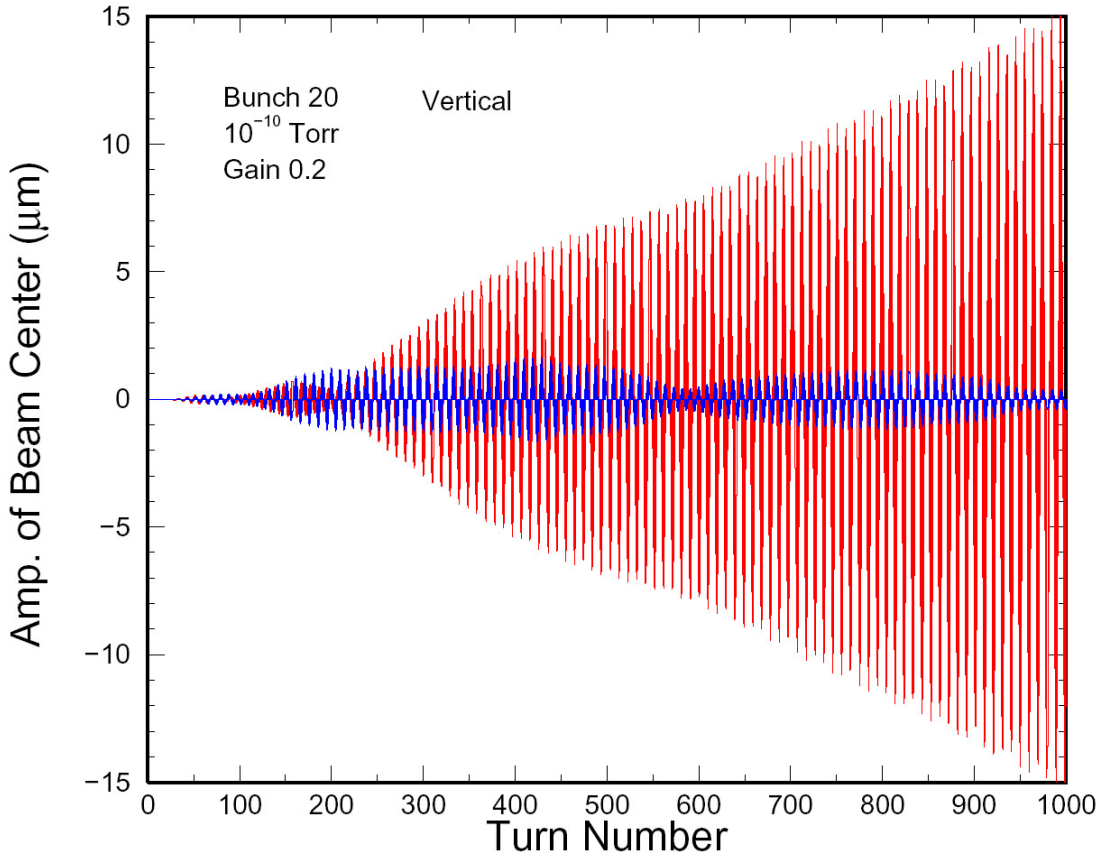

Figure 4.2a: (color) Vertical amplitudes of the 20th bunch in the train for the first 1000 turns at vacuum pressure 10^{-10} Torr without and with feedback of gain 0.2. The growths have been much slower than when the pressure was 10^{-8} Torr. Feedback with a gain of 0.2 controls the oscillation of the bunch centers to within the rms bunch size.

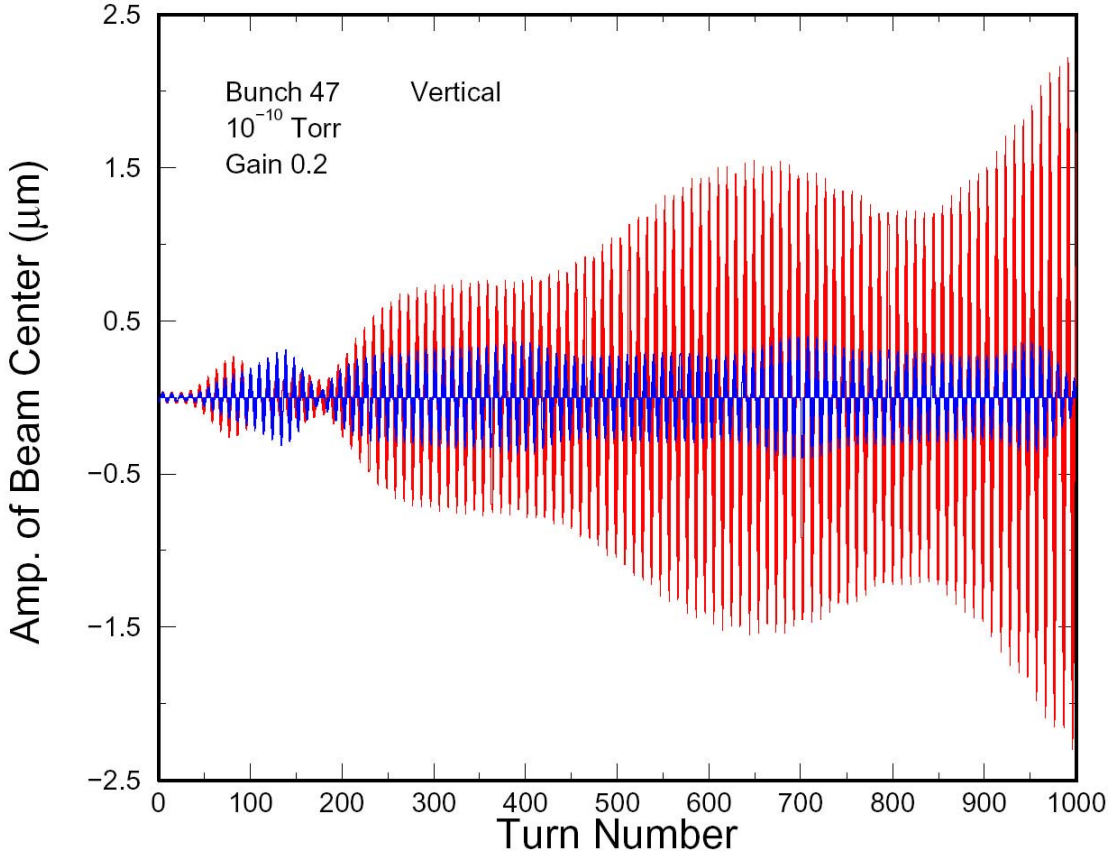

Figure 4.2b: (color) Vertical amplitudes of the 47th bunch in the train for the first 1000 turns at vacuum pressure 10^{-10} Torr without and with feedback of gain 0.2. The growths have been much slower than when the pressure was 10^{-8} Torr. Feedback with a gain of 0.2 controls the oscillation of the bunch centers to within the rms size of the bunches.

So far we have been looking at only two bunches in a particle train. In order to have better statistics, we average over all 60 trains. For this we define the offset emittance $\varepsilon_{offset} = y^2_{beamcenter} / \beta_y$, and normalize it with respect to the vertical emittance of the beam. The averages of this normalized offset emittance over 60 trains are shown in Figs. 4.3a and 4.3b. The first figure is for bunches 7, 14, 21, 28, 35, 42, and 46 at vacuum pressure of 0.1 nTorr while Fig. 4.3b shows the same but with feedback of gain 0.20 turned on.

We find that the growth without feedback increases with bunch position, but it does not scale with the square of bunch position as postulated in Ref. [4.6]. With feedback turned on, the offset emittance is damped to within 20% of the beam vertical emittance. The vertical offset is within 10% of the vertical beam size.

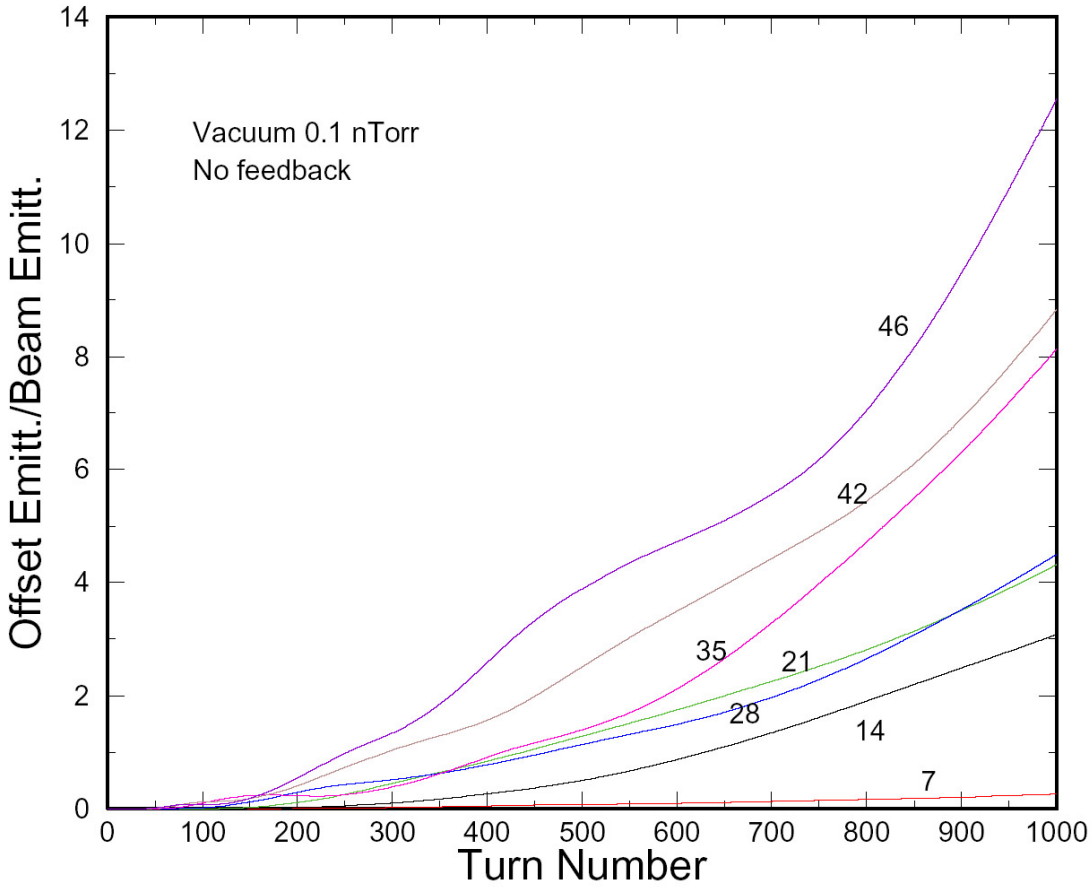

Figure 4.3a: (color) Normalized offset emittance of bunches 7, 14, 21, 28, 35, 42, and 46, averaged over 60 trains without feedback at vacuum pressure of 0.1 nTorr. It is evident that the growth without feedback increases with bunch position. With feedback of gain 0.20, the offset emittance is controlled to within 20% of the vertical emittance of the beam.

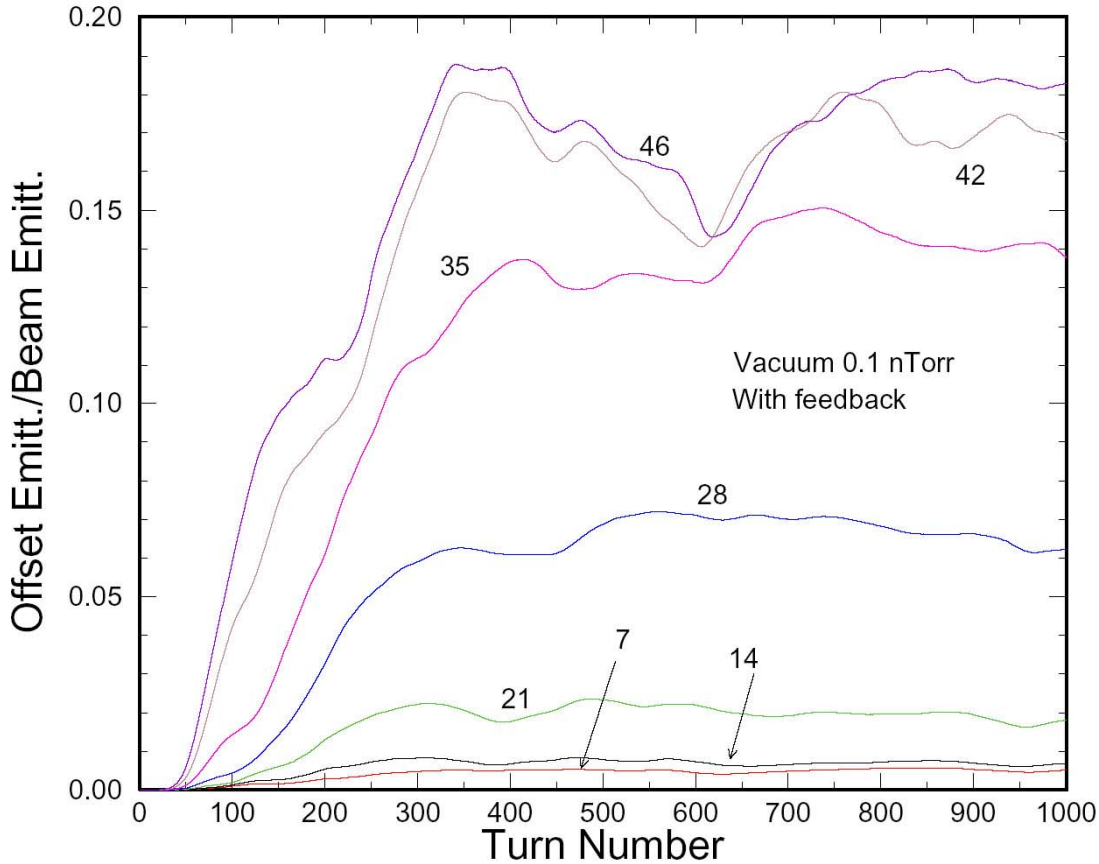

Figure 4.3b: (color) Normalized offset emittance of bunches 7, 14, 21, 28, 35, 42, and 46, averaged over the 60 trains with feedback at vacuum pressure of 0.1 nTorr. It is evident that the growth without feedback increases with bunch position. With feedback of gain 0.20, the offset emittance is controlled to within 20% of the vertical emittance of the beam.

Note that radiation damping has not been included in these simulations. The radiation damping time is approximately 1400 turns. Thus when radiation damping is considered, the offset emittance will be much less. The amplitudes of oscillation of bunches are simulated to be recorded at a beam-position motion but at different time.

Now let us look at the motion of all 2820 bunches in a snapshot. To convert to bunch amplitudes in a snapshot, the BPM values for the jth bunch in the kth train must be multiplied by the betatron phase $\exp\left\{i2\pi\left[57\left(k-1\right)+\left(j-1\right)\right]\nu_y/N_{sp}\right\}$. For simplicity, the simulation assumes 60 trains of 47 bunches, with each train followed by 10 empty bunch spacings. As a result, the total number of bunch spacings around the ring is $N_{\text{sp}} = 60 \times 57 = 3420$.

We next calculate the Fourier transform for each turn by multiplying the snapshot amplitude by[4] $\exp[-i2\pi m/N_{sp}]$ and summing over the bunch spacing m from 0 to $N_{sp} - 1$. The results in the vertical at the 50th, 250th, 500th, 750th and 1000th turns are shown in Fig. 4.4a (Fig. 4.4b) without (with) feedback of gain 0.20.

According to the analysis of Chao [4.8], the resonant modes occur at $\ell = \nu_y - Q_{iy}$ where $\omega_{iy} = Q_{iy}\omega_0$ is the ion bounce angular frequency. Because the imaginary part of the amplitude is not monitored at the BPM, the Fourier transform results in another mirror resonance at $\ell = \left(\nu_y - Q_{iy}\right) + N_{sp}$. These two resonances do appear for each snapshot in Fig. 4.4, and their mode numbers add up to ~3510, which is exactly $N_{sp} + 2\nu_y$ as expected ($\nu_y = 45.1$).

We identify the left resonance at $\nu_y + Q_{iy}$ and the right at $(\nu_y - Q_{iy}) + N_{sp}$. Since they correspond to 815 and 2895 at the 50th turn, we obtain $Q_{iy} = 775$, which agrees well with $Q_{iy} = 716$ obtained from Eq. 4.23. Without feedback, as time goes on, the resonances shift to lower frequencies while their amplitudes become larger. This just reflects the evolution of the resonant beam-ion coupled oscillation with the beam size becoming larger and larger. With feedback turned on, we see that Q_{iy} does not increase any more after 250 turns and so are the resonant amplitudes. This reflects the fact that equilibrium has been reached in the presence of feedback, so that both the beam size and the oscillation amplitude do not increase anymore.

[4] If we multiply by $\exp[+i2\pi m/N_{sp}]$ instead, the two resonant modes in the mode spectrum will be at $\ell = Q_{iy} - \nu_y$ and $N_{sp} - (\nu_y + Q_{iy})$. Note that the two resonances in the Fourier transform correspond to the same mode.

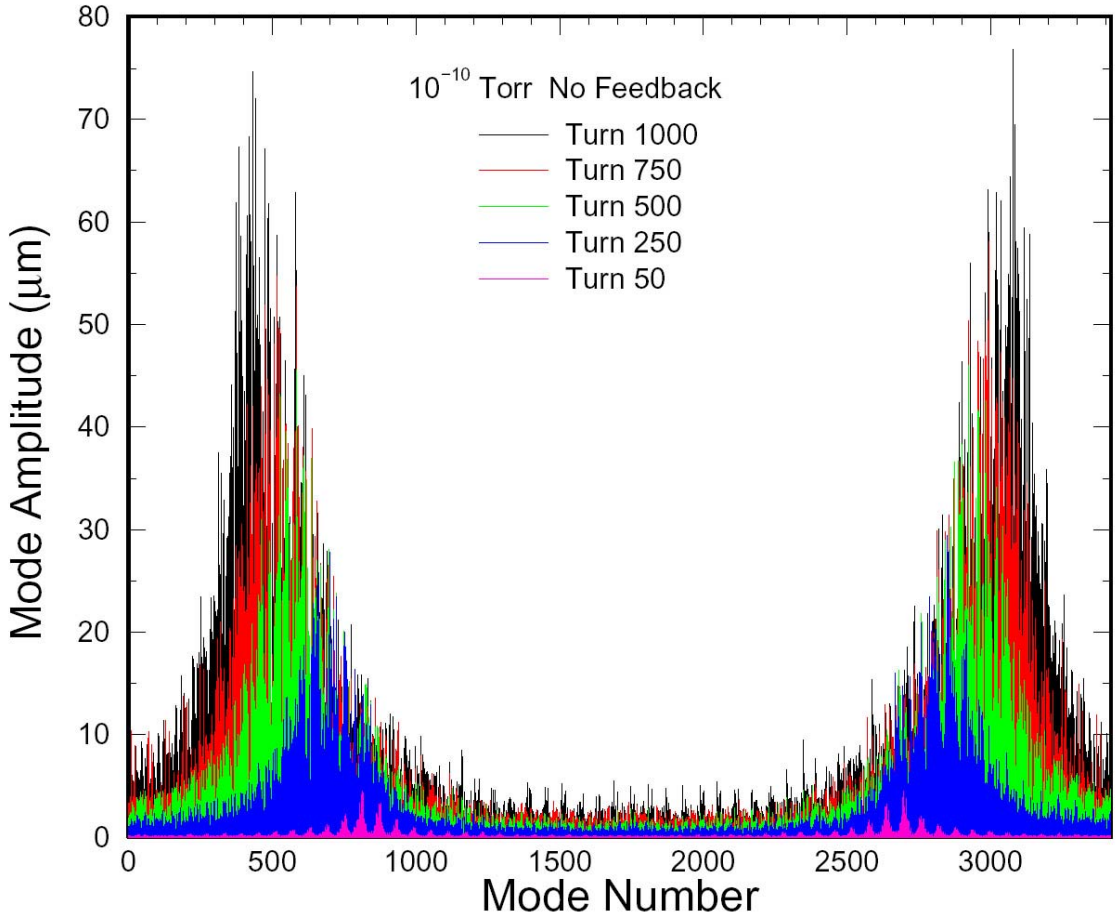

Figure 4.4a: (color) Snapshot mode spectra are shown for the 50th, 250th, 500th, 750th and 1000th turns at vacuum pressure 10^{-10} Torr without feedback. The resonant modes correspond to $\nu_y + Q_{iy}$ and $(\nu_y - Q_{iy}) + N_{sp}$. Without feedback the resonant amplitudes increase in time and the ion-bounce frequency decreases indicating that that the beam size increases.

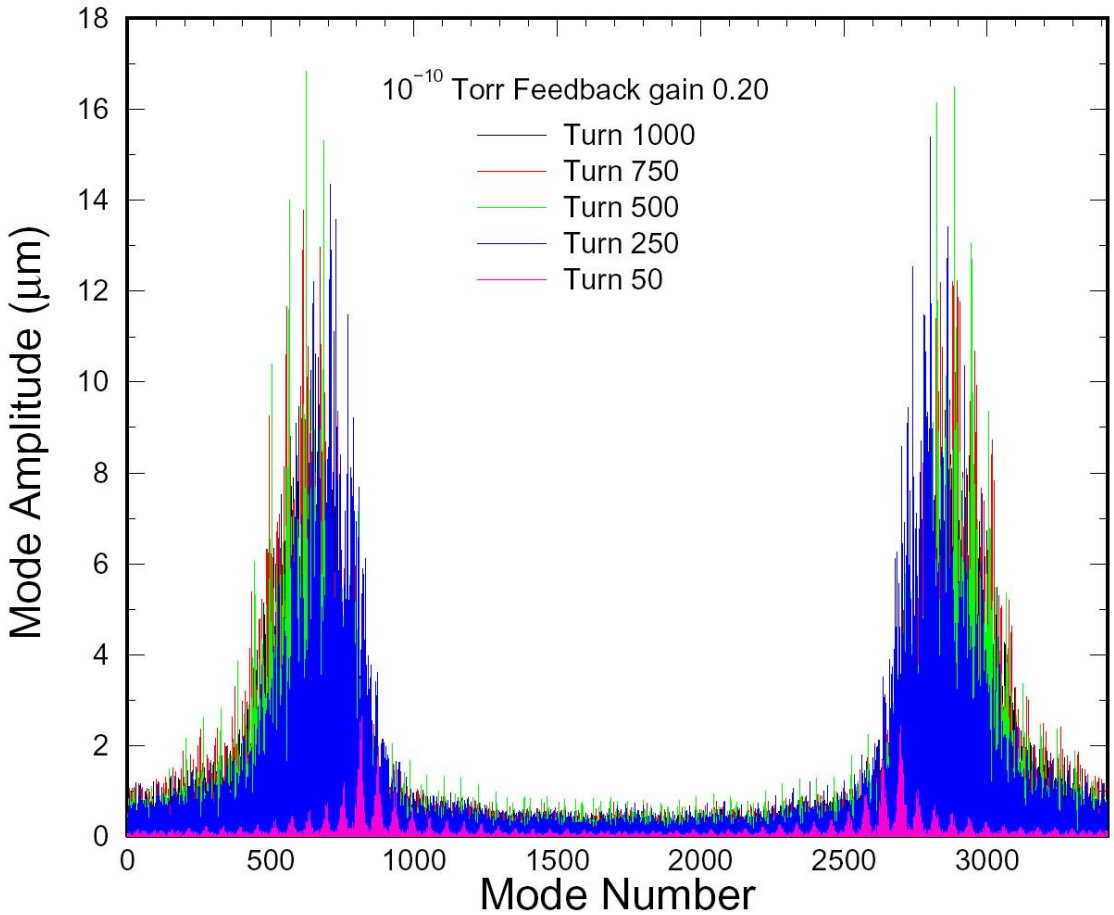

Figure 4.4b: (color) Snapshot mode spectra are shown for the 50th, 250th, 500th, 750th and 1000th turns at vacuum pressure 10^{-10} Torr with feedback gain 0.2. The resonant modes correspond to $\nu_y + Q_{iy}$ and $(\nu_y - Q_{iy}) + N_{sp}$. With feedback, both the resonant amplitudes and ion-bounce frequency reach saturation.

5. Controls and instrumentation

Tolerances and Correction Procedures

In this section we follow similar discussions in the TESLA design reports,[5.1, 5.2] modified to follow the different parameters of the present report.

The vertical equilibrium emittance obtained in the damping ring is determined by the quadrupole, sextupole and BPM alignment tolerances, and by the orbit correction procedures that are used. The ILC damping rings require a normalized vertical emittance $\varepsilon_{N,\,L,rms}$ of less than ~0.02μm. At 5 GeV this implies a geometric emittance of $\varepsilon_{L,Geom} <$ 2pm.

The sensitivity of the vertical beam parameters to errors in the quad and sextupole alignments are given by: [5.3]

$$\frac{\langle y^2 \rangle}{\langle \sigma_y^2 \rangle} = \frac{\langle \Delta Y_q^2 \rangle}{8\varepsilon_y (\sin \pi\nu_y)^2} \sum_{\text{quads}} \beta_y (k_q L_q)^2$$

$$\frac{\Delta\varepsilon_y}{\langle \Delta\Theta_q^2 \rangle} = \frac{J_x}{J_y} \frac{1 - \cos 2\pi\nu_x \cos 2\pi\nu_y}{(\cos 2\pi\nu_x - \cos 2\pi\nu_y)^2} \varepsilon_x \sum_{\text{quads}} \beta_x \beta_y (k_q L_q)^2 + J_z \frac{\sigma_\delta^2}{(\sin \pi\nu_y)^2} \sum_{\text{quads}} \beta_y \eta_x^2 (k_q L_q)^2$$

$$\frac{\Delta\varepsilon_y}{\langle \Delta Y_s^2 \rangle} = \frac{J_x}{4J_y} \frac{1 - \cos 2\pi\nu_x \cos 2\pi\nu_y}{(\cos 2\pi\nu_x - \cos 2\pi\nu_y)^2} \varepsilon_x \sum_{\text{sexts}} \beta_x \beta_y (k_s L_s)^2 + J_z \frac{\sigma_\delta^2}{4(\sin \pi\nu_y)^2} \sum_{\text{sexts}} \beta_y \eta_x^2 (k_s L_s)^2$$

Here J_{ix}, J_y, J_z are the damping partition numbers, (k_q, L_q) and (k_s, L_s) are the ring quad and sextupole strengths, (β_x, β_y, η_x, ν_x, ν_y) are the usual betatron functions, dispersion and tunes. $\langle \Delta\Theta_q^2 \rangle$ is the rms angle error in the quads, $\langle \Delta Y_s^2 \rangle$, $\langle \Delta Y_q^2 \rangle$ are the rms alignment error in the sextupoles and quadrupoles, respectively, $\langle \sigma_y^2 \rangle$ is the rms vertical beam size squared and σ_δ^2 is the rms $\delta p/p$ squared. $\langle y^2 \rangle$ is the resulting closed orbit error and $\Delta\varepsilon_y$ is the resulting increase in rms emittance. The expressions in the previous equations determine the quadrupole jitter sensitivity, the quadrupole rotation sensitivity, and the sextupole alignment sensitivity. [5.4]

As evaluated by Wolski [5.5], the present damping ring design has a quadrupole jitter sensitivity that is ~2.5× less than the baseline Tesla Damping Ring, the quadrupole rotation sensitivity is ~1.5× smaller and the sextupole alignment sensitivity is ~3.6× smaller, mostly because of the smaller circumference.

These sensitivities are not directly interpreted as survey alignment tolerances, since achieving the desired vertical emittance will require correction of the dispersion and the betatron coupling, and detailed simulation studies of the correction procedure.

For the TESLA design report, the errors and correction were simulated using the PETROS code, which has been benchmarked by observations in the HERA electron ring.[5.1] A set of initial alignment tolerances were obtained, and these tolerances are displayed in Table 5.1. Note that tolerances for wiggler/BPM positions are at the μ scale and will require local beam-based averaging adjustment. By extrapolation, these tolerances should also be acceptable in the present ring, and probably can be relaxed by a factor of ~2. A more detailed study with new simulations should be developed for a more precise evaluation.

Element	Error Type	Tolerance (rms)
Quadrupoles (arcs)	Transverse position	0.1 mm
(straight sections)	Transverse position	0.2 mm
	Roll angle	0.2 mrad
Sextupoles	Transverse position	0.1 mm
	Roll angle	0.5 mrad
Dipoles	Roll angle	0.2 mrad
BPM's vs. quads	Transverse position	0.1 mm
BPM resolution	Transverse position	0.01mm
BPM resolution (wiggler, averaging mode)	Transverse position	0.001mm

Table 5.1: Damping ring tolerances (based on TDR analysis, not relaxed for lesser DR sensitivity).

An important question concerns long-term orbit stability and emittance increase. From the experience at HERA, [5.5] a diffusion-like orbit drift caused by uncorrelated slow ground motion must be considered. Steering the orbit back to the reference orbit ~every 20 minutes should be sufficient to control this effect.

Beam-Gas and Intrabeam Scattering

Incoherent scattering processes set upper limits on the beam lifetime and lower limits on the beam emittances in the damping ring. The largest contribution to vertical emittance growth is due to elastic Coulomb scattering with gas nuclei. The rms emittance growth from this effect is given by: [5.6]

$$\gamma\,\Delta\varepsilon_{y,BG} = \frac{\pi c r_e^2 \tau_y}{\gamma}\left\langle \beta_y N_{gas} \right\rangle l_{sc}\,,$$

where N_{gas} is the number density of gas molecules and l_{sc} is the Coulomb scattering logarithm ($l_{sc} \cong 5$). With $P_{gas} < 10^{-8}$ mbar, the resulting increase in emittance, $\Delta\varepsilon_{y,BG}$. is < ~10% of the design value. This rms emittance formula exaggerates the effect on the core of the beam, since the growth comes from relatively few particles scattered to larger angles, and the distribution is very non-Gaussian. The luminosity loss would be much less than indicated by the rms values, and should be practically negligible.[5.7]

Intrabeam scattering (IBS) affects both the transverse and longitudinal emittances, and adds an emittance growth rate which opposes the radiation cooling term. The IBS-growth times can be estimated using the formulae in ref. [5.8]. At the damping ring parameters, we find: $\tau_{z,IBS} \cong 3$s, $\tau_{x,IBS} \cong 0.25$s, and $\tau_{z,IBS} \cong 20$s. Even the smallest of these growth times (τ_x) is much greater than the radiation damping time, and only a small correction occurs.

The most important limitation on the beam lifetime in electron/positron storage rings at high particle densities is due to the Touschek effect. This lifetime is several hours in the damping ring, so it will not be a limitation for operational use of the damping ring. The

effect should not even be a strong limitation for diagnostic and commissioning operation of the damping ring in long-term storage mode.

6. Fourier kicker system

Introduction

It is interesting to consider a design in which a pulsed kicker is replaced by a broadband RF system whose amplitudes, frequencies, and phases correspond to the Fourier components of a periodic, narrow pulse. Instead of energizing the system only when a bunch was about to be injected or extracted, the device would run continuously. This might allow the frequencies, phases, and relative amplitudes of the various Fourier components to be determined (and maintained) with great precision. With a properly chosen set of parameters, the system would kick every M^{th} bunch in the damping ring, leaving undisturbed the intervening (M - 1) bunches. Injection (or extraction) of an entire bunch train would be completed by the end of the Mth orbit through the system.

Other types of kicker are also under consideration; the damping ring lattice has sufficient length in one of the straight sections to accommodate any one of several varieties of kicker. We will focus on one kicker scheme, currently under study at Fermilab. In our discussions we will assume the timing structure for the beam shown in Table 6.1.

Parameter	Value
Main linac RF frequency	1.300 GHz (442 × linac bunch frequency)
Main linac bunch spacing	340 ns (1/442 of linac RF frequency)
Number of main linac bunches	2820
Number of damping ring bunch trains	60
Bunches per train	47
Inter-train gap following trains 1-59	10 damping ring bunch spacings (~60.7 ns)
Inter-train gap following train 60	11 damping ring bunch spacings (~66.8 ns)
Inter-bunch separation	~6.07 ns (main linac bunch spacing / 56)
Train length (including gap), trains 1-59	340 ns = main linac bunch spacing
Train length (including gap), train 60	~346.1 ns = 57 × bunch spacing
Damping ring orbit period	~20,406.1 ns (60 × 340 + 1 inter-bunch gap)
Damping ring orbit circumference	~6.12 km
Damping ring RF frequency	~494.1 MHz (168 × linac bunch frequency)
Kicker center frequency	~1.647 GHz (10 × 1/ DR bunch spacing)
Kicker bandwidth	±10% of center frequency

Table 6.1: damping ring parameters assumed in kicker studies

General Discussion of a Fourier-Series Kicker System

A Fourier-series kicker system could be installed in a bypass section of the damping ring, as shown schematically in Figure 6.1. During injection, a deflector system would route the beam through the bypass. Once injection was completed, each deflector could be turned off during the passage of a gap between the last and first bunches in the orbiting train. The train would then orbit in the damping ring, bypassing the kicker. At extraction, the deflectors would be energized again, routing the beam through the kicker for extraction.

How many Fourier components would be required to synthesize a kicker pulse? The required kicker field integral is [6.1] 100 Gauss-meters with an accuracy of 0.07 Gauss-meters. The kicker's residual field integral when "off" should be less than 0.07 Gauss-meters. An idealized kicker pulse train of pulses with width δ and period T is shown in Figure 6.2. Since the train is an even function of time, its Fourier expansion is

$$\text{Impulse} = \sum_{k=0}^{\infty} A_k \cos\left(k\omega_0 t\right); \quad \omega_0 = \frac{2\pi}{T}.$$

Naturally, the values of the coefficients A_k depend on the pulse shape, but components with periods that are long compared to the pulse width δ will appear with coefficients that are approximately equal. The magnitude of coefficients A_k for high frequency

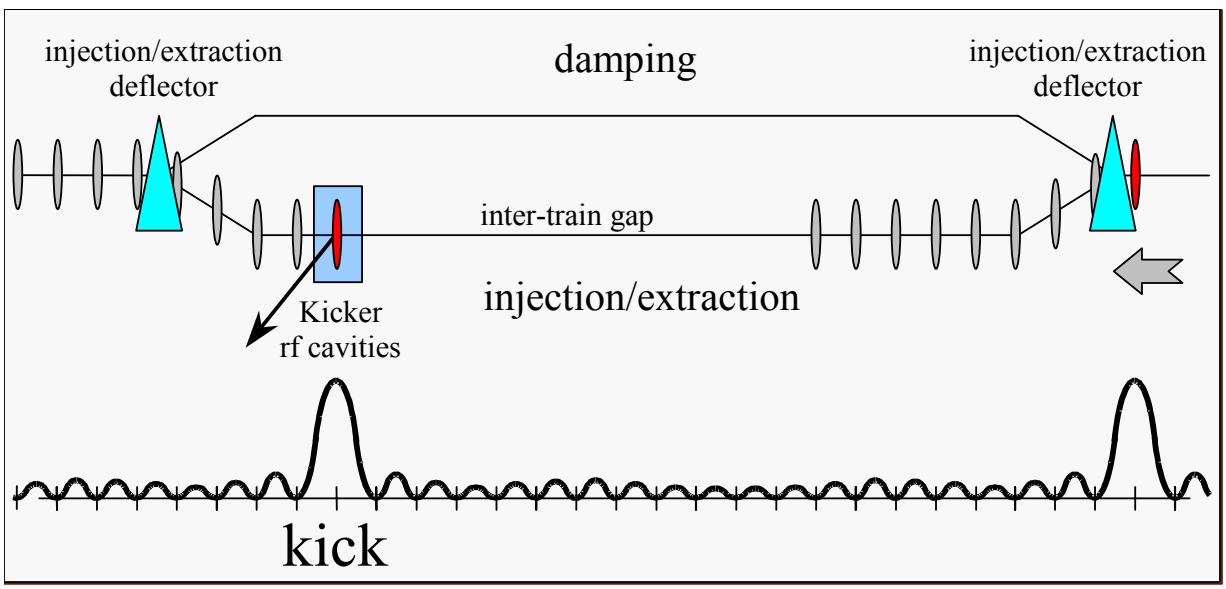

Figure 6.1. Schematic diagram of a damping ring using an RF cavity kicker system located in a bypass section. Injection/extraction deflectors are off during damping, allowing the beam to pass through a section of the ring which does not include the kicker. Deflectors are energized during the passage of a gap between the last and first bunch trains for injection and extraction, routing the beam through the kicker.

components will decrease with increasing k. For a train of Gaussian pulses, where δ is the rms pulse width, the Fourier expansion is [6.2]

$$\text{Impulse} = 1 + 2\sum_{k=1}^{\infty} e^{-\left(k\omega_0\delta\right)^2/2} \cos\left(k\omega_0 t\right).$$

A single pulse $e^{-(t/\delta)^2/2}$ will drop below .07% for $t \geq 3.81\delta$. For example, to accommodate damping ring and linac bunch spacing of 6 ns and 340 ns respectively, the pulses would need rms widths below $\delta = 1.57$ ns.

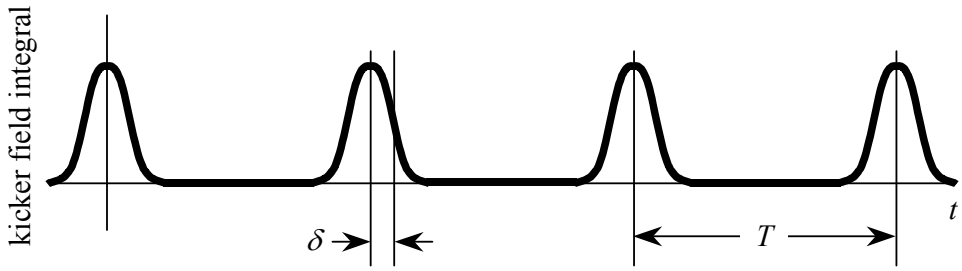

Figure 6.2. Idealized kicker pulse train. Each pulse has width δ. The pulse repeat period is T.

The magnitude of the Fourier coefficients $A_k = e^{-(k\omega_0\delta)^2/2}$ drops below .01% when $k = 148$, so a kicker system of this sort would require the construction of a large number of cavities. It is likely that controlling the relative amplitudes in the cavities (so that the proper Fourier sum is obtained) would pose a difficult technical challenge!

This naïve approach—that the kicker fields should be close to zero at all times except when a bunch is about to be kicked—places demands on the kicker system that are unnecessary. Since the arrival time of bunches at the kicker is precisely known, we can consider an alternative approach in which the sum of Fourier components generates a field integral that is zero as a bunch passes through the kicker, but can be non-zero at other times. TESLA bunch lengths are 6mm in the damping ring, both at injection and extraction. [6.1] As long as the change in the field integral is small during the 20 ps time interval between the arrival of the head and tail of a bunch at a cavity center, the effects of ripple when the cavities are empty should be unimportant.

Let us analyze the properties of a kicker made from N cavities tuned to oscillate with identical amplitudes, and at frequencies which are integer multiples of 2.94 MHz (1/340 ns). To simplify calculation, we will assume that a constant impulse, with half the strength of the individual cavity amplitudes, is applied to bunches just before they enter the kicker cavities. The summed field integral is

$$\text{Impulse} = A\left[\frac{1}{2} + \sum_{k=1}^{N} \cos\left(k\omega_0 t\right)\right]; \quad \omega_0 = \frac{2\pi}{340\text{ ns}}.$$

This can be evaluated [6.3] analytically:

$$A\left[\frac{1}{2} + \sum_{k=1}^{N} \cos\left(k\omega_0 t\right)\right] = A\left[\frac{\sin\left[\left(N + \frac{1}{2}\right)\omega_0 t\right]}{2\sin\left(\omega_0 t/2\right)}\right].$$

Two notable features about this expression are that its zeroes are evenly spaced, and that it has a peak of height $N + ½$ (instead of a zero) whenever its denominator is zero. The even spacing of its zeroes makes this an interesting candidate for a kicker system.

A graph of the field integral for $A = 6.5$ Gauss-meters and $N = 16$ is shown in Figure 6.3.

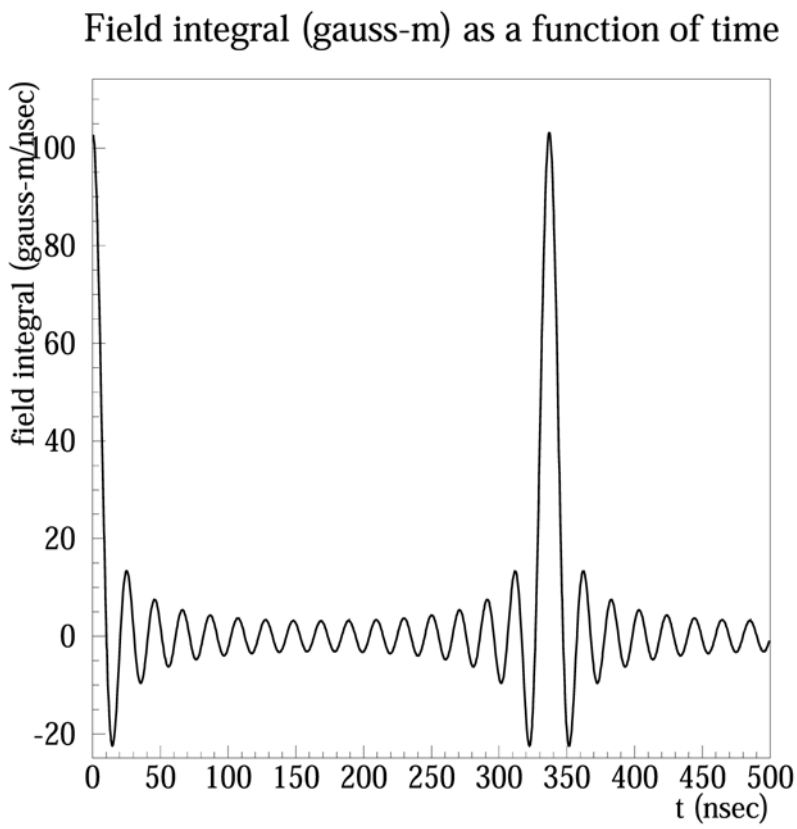

Figure 6.3. Field integral (Gauss-meters) *vs*. time (ns) in a 16-element system. Bunches 1 and 34 are kicked, while damping ring bunches 2 through 33 pass through the kicker during the zeroes of the field integral.

There are $2N$ zeroes between the peaks at 0 ns and 340 ns. If a bunch passed through the kicker during each of its zeroes, as well as during its kicking pulse this would correspond to a reduction in damping ring bunch spacing relative to linac bunch spacing by a factor of $2N + 1$. For $N = 16$, this would decrease the required damping ring circumference by a factor of two relative to the size specified in the TESLA *Technical Design Report*. [6.1]

The time derivative of the summed field integral is shown in Figure 6.4. The derivative's value at a zero crossing of the field integral is

$$\frac{d}{dt}\left(\text{Impulse}\right) = \pm\left(N + \tfrac{1}{2}\right)\frac{A\omega_0}{2\sin\left(\omega_0 t/2\right)};$$

as can be seen in the figure, the derivative switches sign at successive zeroes in the field integral and is largest for the zero crossing closest to the pulse which kicks a bunch.

The 6 mm rms bunch width in the damping ring corresponds to a flight time of 20 ps. A slope at a zero crossing in the field integral of 2 Gauss-meters/ns would produce a kick error of 0.04 Gauss-meters, somewhat smaller than the tolerance of 0.07 Gauss-meters. However, the number of passes a bunch makes through the kicker system ranges from 1 (for a bunch which is kicked immediately) to $2N + 1$ (for a bunch which is kicked during the train's last orbit through the kicker system). As a result, an analysis of the effects associated with finite bunch length will need to take into account the cumulative effects of multiple passes through the kicker and the synchrotron oscillations of an electron (or positron) in the direction of motion of the bunch as the train travels through the damping ring.

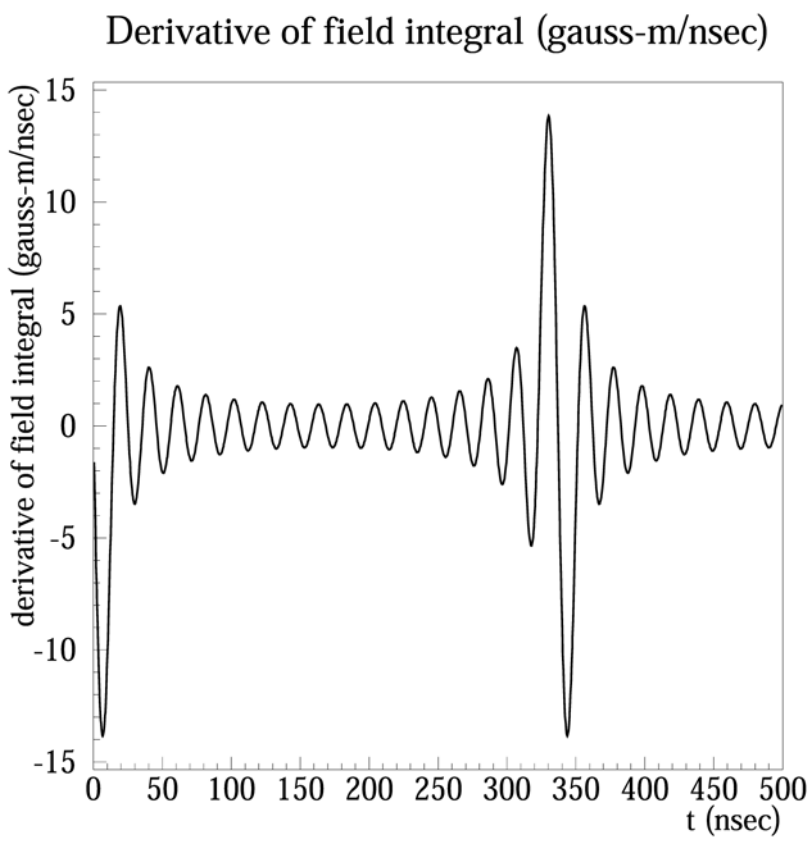

Figure 6.4. Time derivative of field integral (Gauss-meters per ns) *vs*. time (ns) in a 16-element system.

The problem of head-tail effects on bunches due to the non-zero slope at the zeroes in the previously described impulse function can be eliminated by employing an impulse function whose magnitude <u>and</u> slope are zero when unkicked bunches pass through the kicker. An example would be

$$\text{Impulse} = A\frac{\sin^2\left(N\omega_0 t/2\right)}{\sin^2\left(\omega_0 t/2\right)} \quad \left(\omega_0 = \frac{2\pi}{340\text{ ns}}\right)$$

whose Fourier components a_k decrease linearly, becoming identically zero when $k > N$. A bunch spacing of 6.07 ns requires $N = 56$, so the frequency range of this device is quite broad, spanning the interval 2.94 MHz to 164.7 MHz.

Modulating the kicking impulse by a high frequency signal so that its center frequency is raised considerably can reduce the fractional bandwidth of the device. We have been studying the possibility of designing a kicker whose field integral is

$$\text{Impulse} = A\frac{\sin^2\left(N\omega_0 t/2\right)}{\sin^2\left(\omega_0 t/2\right)}\cos\left(\Gamma N\omega_0 t\right) \qquad \left(N = 56 \text{ and } \Gamma N = 560\right).$$

The impulse as a function of time is shown in Figure 6.5. This device would have a center frequency of 1.647 GHz and contain frequencies in an interval ±164.7 MHz around 1.647 GHz. Interestingly, the amplitudes of the Fourier components decrease linearly from a maximum at the center frequency, becoming (and remaining) identically zero ±164.7 MHz away from 1.647 GHz.

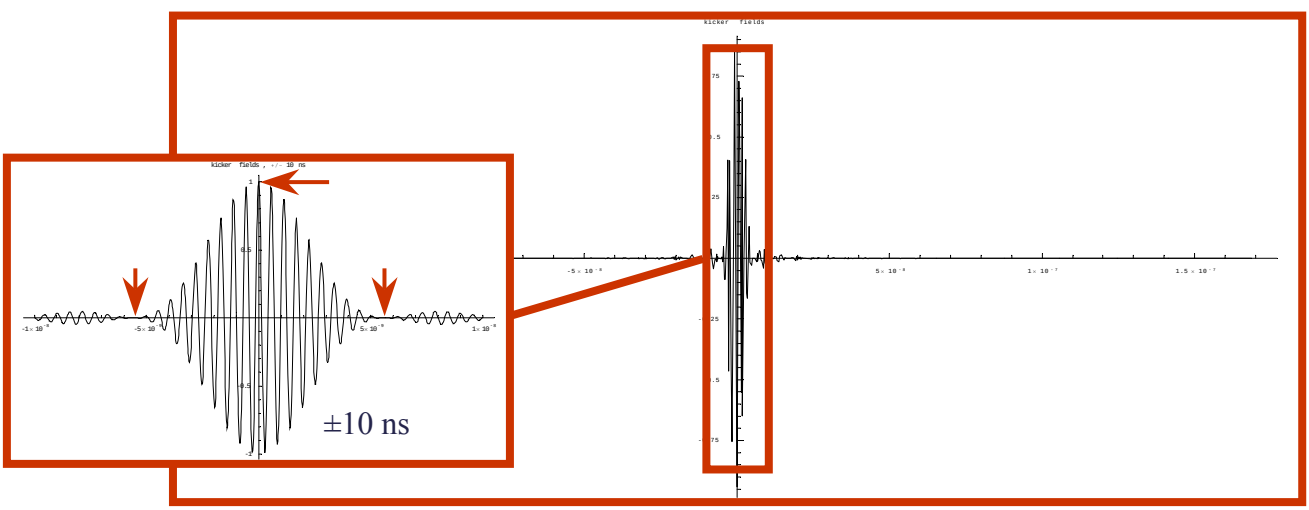

Figure 6.5. Impulse as a function of time for a high-frequency modulated kicker. The inset shows a ± 10 ns full scale time interval while the larger figure represents a full 340 ns linac inter-bunch interval. In the inset, arrows indicate the arrival times of the kicked bunch and adjacent unkicked bunches.

Other impulse functions could be chosen as long as they possess the general feature of periodic zeroes with zero slopes.

Mode of Operation During Extraction and Injection

We have been assuming that the damping ring's 2820 bunches will be grouped into 60 distinct trains separated by inter-train gaps. Each train contains 47 bunches separated by ~6.07 ns. The gaps following all but the last train are ~60.7 ns long; this last gap is reduced to ~54.6 ns. With this timing arrangement, the last bunch in one train arrives at the kicker 340 ns after the last bunch in the previous train during an orbit of the damping ring.

The kicker ejects the last bunch in each train; because of the shortened gap after the last train, the beam's next orbit presents what had been the next-to-last bunch to the kicker in time for it to receive an extraction impulse.

The orbital period for the beam is the sum of the lengths for all the trains, including their trailing inter-train gaps. This is ~20,394 ns. Extraction of the entire beam requires 47 orbits.

When it is time to begin extracting beam from the damping ring, the deflectors are energized as the inter-train gap following the last train passes through a deflector; the deflectors remains on for the duration of the extraction cycle.

The process for injection is a time-reversed version of extraction: bunches are kicked on orbit to join the partially formed trains as the (newly arrived) last bunch in the train.

Effect of Bunch Arrival Time Error at the Kicker

The consequences of an error in arrival time of a bunch at the kicker are more important for a bunch that is being injected (or extracted) by the kicker than on bunches passing through when the net impulse is zero.

The field integral pulse that ejects a bunch is parabolic near its peak. In the example discussed above, its shape is dominated by the modulating cosine:

$$\text{Impulse} = A\frac{\sin^2\left(N\omega_0 t/2\right)}{\sin^2\left(\omega_0 t/2\right)}\cos\left(\Gamma N\omega_0 t\right) \approx AN^2\left[1-\frac{\left(\Gamma N\omega_0\right)^2}{2}t^2\right].$$

The value of the coefficient of the quadratic term is approximately $1/(137\text{ ps})^2$. As a result, a timing error of 10 ps (comparable to half the length of a bunch) yields a 0.5% reduction in the strength of the impulse. Some sort of compensation along the extraction line downstream of the kicker will be necessary to correct for this.

The effect is considerably less pronounced for bunches which are not meant to be deflected by the kicker. The impact of an arrival time error is greatest for bunches immediately before and after the bunch which is kicked. In this case, the $\sin^2(N\omega_0 t/2)$ numerator dominates the shape of the impulse and the effect is considerably less important than it is for the kicked bunch. A timing error of 10 ps yields a few parts per

million reduction in the impulse, while an error of 200 ps causes an error of approximately 0.07%.

Effects Associated With Multiple Passes Through the Kicker

Most bunches pass through the kicker several times after injection, or before extraction. There are a variety of effects which enter into a calculation of the kicker's influence on a bunch which orbits the damping ring several times during the injection/extraction cycle. In the extraction scheme described earlier, a bunch arrives at the kicker one "click" earlier each time it begins its next orbit of the damping ring until finally being ejected. As a result, it passes through the kicker during zeroes which are progressively closer to the kicking peak (located at $t = 0$ in Figure 6.3).

Oscillations of the beam about a closed orbit, as well as the effects of synchrotron oscillations of particles inside the bunch relative to the bunch center will play a role in determining the effects of multiple passes through the kicker. We are currently investigating this.

Summing the Fourier Components

The original conception of the Fourier series kicker employed a separate high-Q RF cavity for each of the individual frequency components. The effect of the cavities would be summed directly by the particle beam directly as it passed through the string of cavities. We also consider a design in which the Fourier components are summed directly inside individual cavities, so that a bunch experiences no deflection at any point as it travels through the kicker unless the bunch is to be extracted.

The technique we are currently studying would use a set of identical low-Q cavities able to support the ±10% bandwidth required to synthesize the kicking pulse from its Fourier representation. The simplest version of this system, in which an amplifier would fill the cavities in a few nanoseconds, would place unacceptable demands on the peak power capacity of the amplifier. Joe Rogers had begun studying a pulse compression scheme for this kind of kicker that would solve the peak-power problem, and we are continuing to develop his ideas.[5]

The idea is similar to that used in some radar systems: waveguides are dispersive, so the relative phases of the various Fourier components in a broadband signal will change as the signal travels down the waveguide. By injecting the proper waveform into the upstream end of the waveguide, it is possible to compress the waveform into a narrow kicking pulse by altering the phases, but not the magnitudes, of the frequency components. As a result, the peak power supplied by the amplifier is not terribly different from the average power. A schematic diagram of the system is shown in Figure 6.6.

---

[5] Joe Rogers, a Professor of Physics at Cornell University, died of cancer in 2004. A gifted scientist and profoundly decent person, we note, and mourn, his untimely passing.

We are currently investigating some of the engineering issues for the kicker in order to better understand its feasibility and its vulnerability to degradation in performance associated with errors in its operating parameters. We have not yet reached the point where it is appropriate to search for an optimum set of operating parameters. As a result, the final device (if it proves possible to build) may differ considerably from the version described below, whose parameters are summarized in Table 6.2.

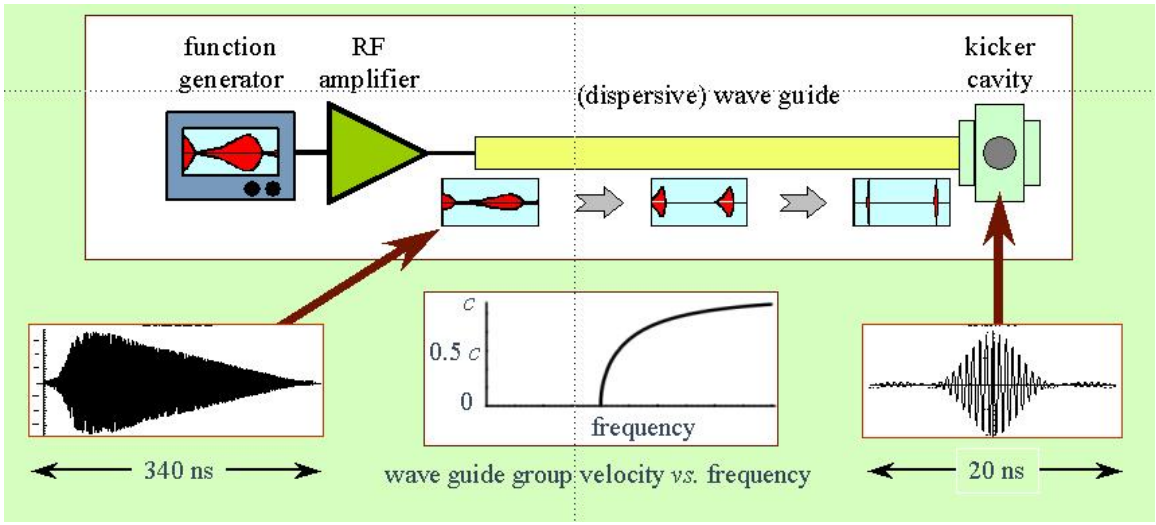

Figure 6.6. Schematic diagram for a pulse compression Fourier series kicker. We are currently studying a system using a 50 m waveguide with 1.3 GHz cutoff frequency.

Parameter	Value
Wave guide length	50 m
Wave guide cutoff frequency	1.300 GHz
RF cavity Q	25
Kicker center frequency	~1.647 GHz (10 × 1/ DR bunch spacing)
Kicker bandwidth	±10% of center frequency
Kicker signal fundamental period	340 ns (linac bunch frequency)
Kicker impulse	100 Gauss-m (more may be necessary for injection)
Kicker precision during extraction	±0.07 Gauss-m (±0.07%)
Kicker off-field error	±0.07 Gauss-m

Table 6.2: kicker parameters

It is instructive to trace the evolution of the signal in Figure 6.6 backwards, beginning at the RF cavity and ending at the function generator. The final signal, supported by the cavity, is shown in Figure 6.7.

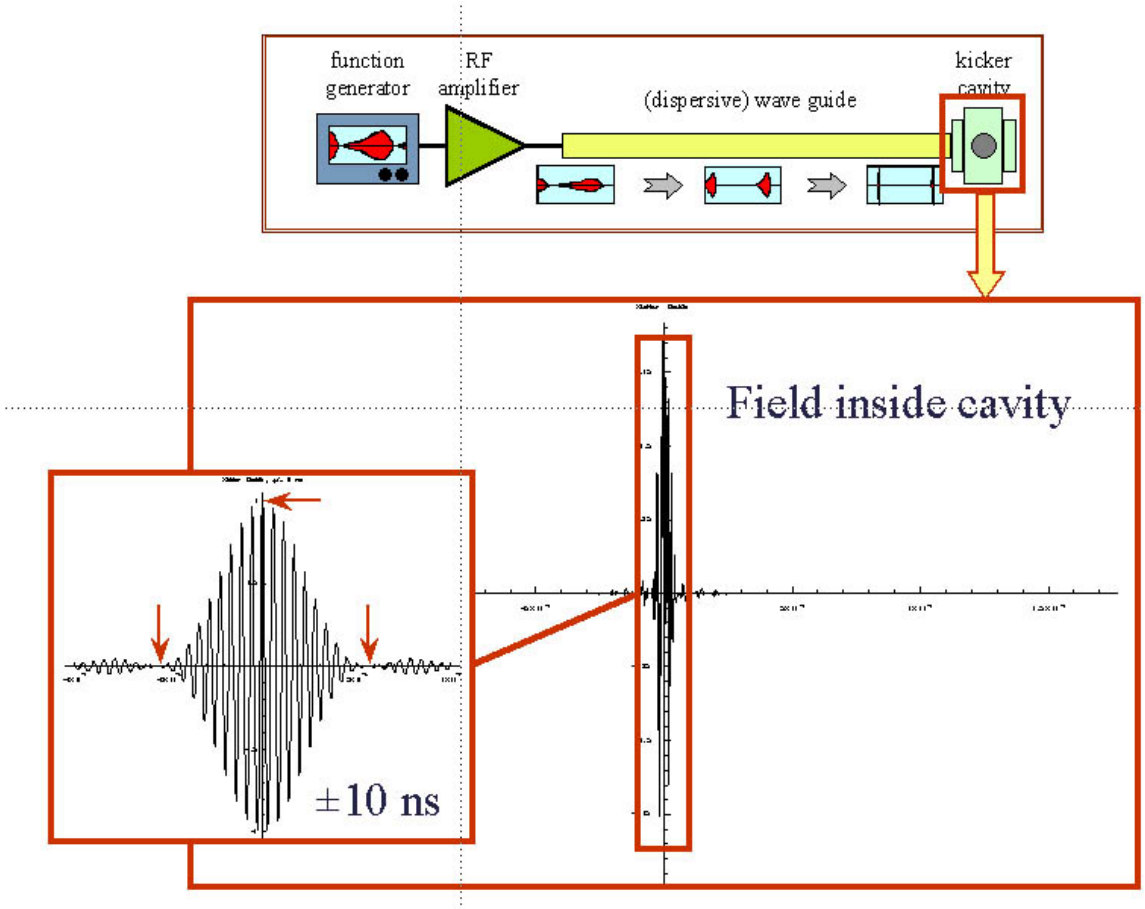

Figure 6.7. Kicker field inside RF cavity. Amplitude, in arbitrary units, has peak value of 1.000. Full scale time range is 20 ns in the inset and approximately 340 ns in the larger figure. Red arrows in the inset indicate arrival times of the kicked bunch (at $t = 0$) and the bunches immediately before and after the kicked bunch.

The functional form of the impulse, as described earlier, is

$$\text{Impulse} = A\frac{\sin^2\left(N\omega_0 t/2\right)}{\sin^2\left(\omega_0 t/2\right)}\cos\left(\Gamma N\omega_0 t\right) \qquad \left(N = 56 \text{ and } \Gamma N = 560\right).$$

The frequency spectrum of the impulse is shown in Figure 6.8. The peak amplitude is 560 times the linac bunch frequency; the amplitudes decrease linearly away from the peak, becoming identically zero ±10% on either side of the peak frequency. The Fourier components are all cosines, and are all in phase so that each has a maximum at $t = 0$.

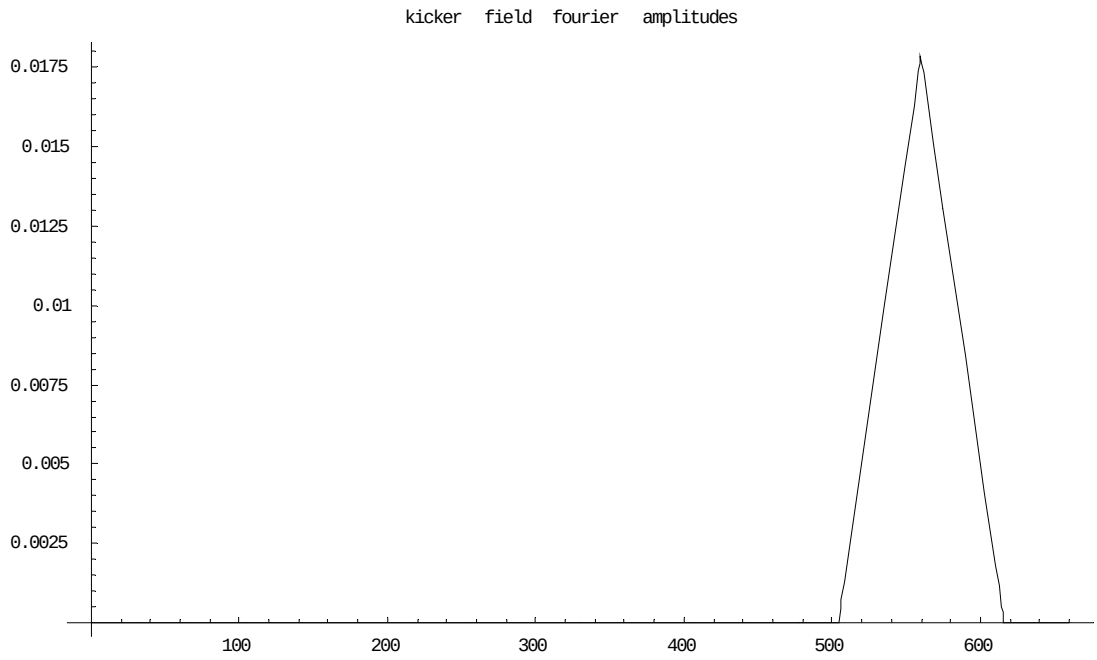

Figure 6.8. Frequency spectrum inside the RF cavity. Frequencies are expressed as multiples of the main linac frequency.

Since the RF cavity's Q is 25, the cavity will accumulate energy sent down the waveguide, supporting a considerably larger instantaneous field than is present at the downstream end of the waveguide. This is shown in Figure 6.9.

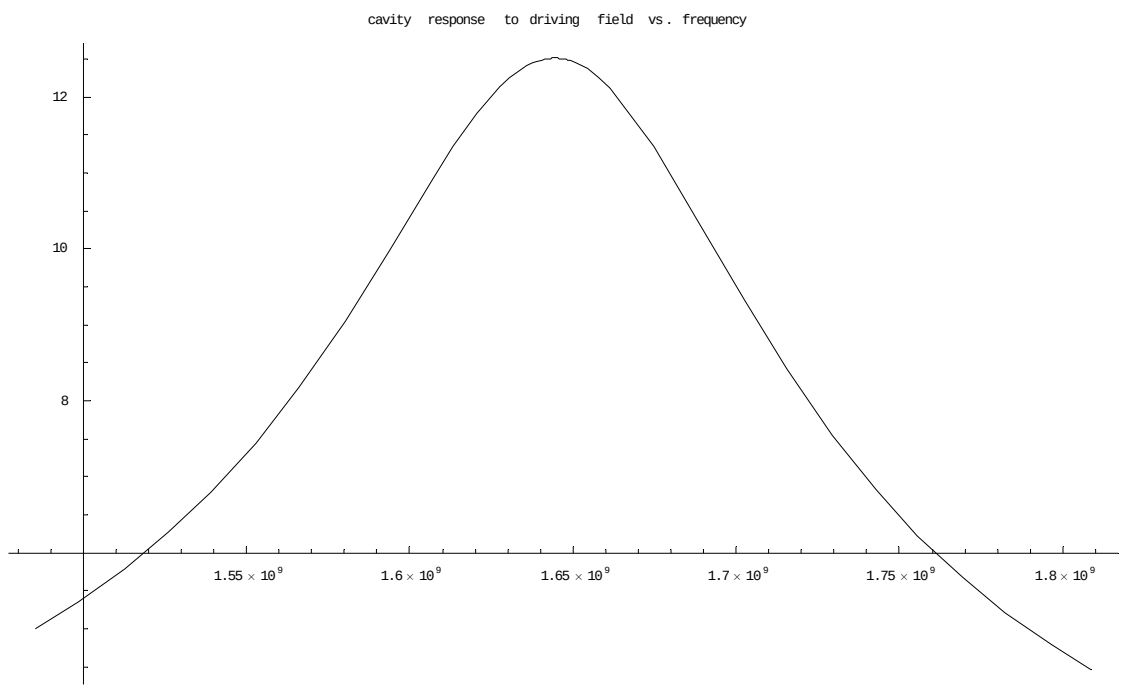

Figure 6.9. Cavity response vs. frequency for full bandwidth of the driving signal. Note the suppressed zero; the plot shows the ratio of the amplitudes for the driving signal at the downstream end of the waveguide and the cavity's kicking field as a function of frequency. The ratio varies from approximately 5 to 12.5.

The phase lag (in degrees) between cavity response and driving signal is shown in Figure 6.10. Not surprisingly, it crosses through 90° at the cavity's center frequency.

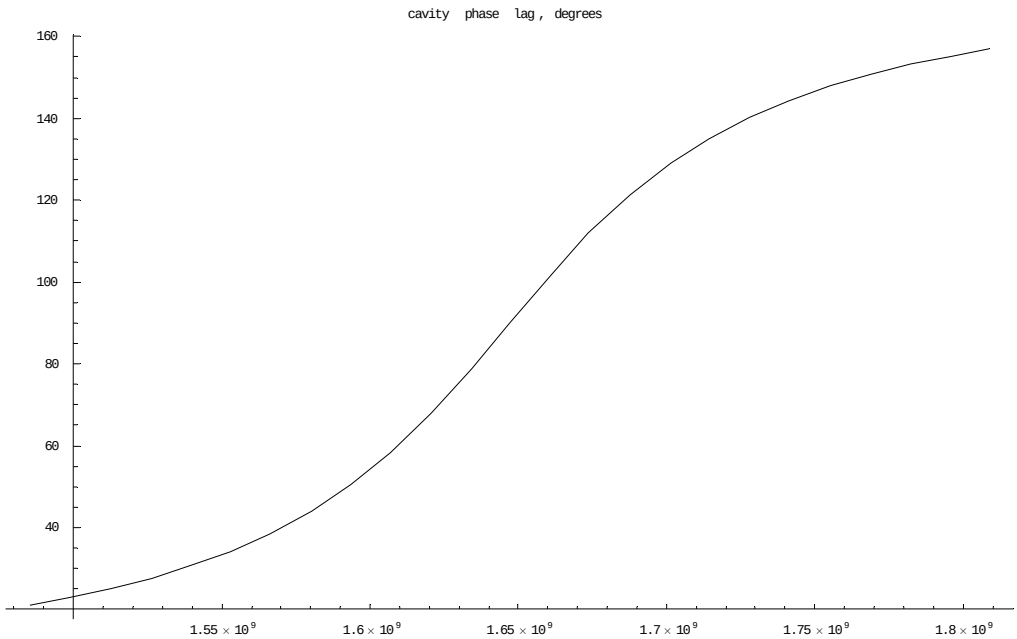

Figure 6.10. Cavity phase lag vs. frequency for full bandwidth of the driving signal. Phase lag is 90° at the cavity's center frequency. The phase lag varies from approximately 20° to 160°.

The signal required to drive the cavity as it appears at the downstream end of the waveguide is shown in Figure 6.11. Note the effects of the phase shift between driving signal and cavity response in removing the signal's symmetry about $t = 0$. In addition, the ability of the cavity to store energy is clearly seen in the large difference in signal amplitudes in the wave guide and the cavity. Most of the energy transported by the waveguide arrives at the cavity during a short time interval.

Because the wave guide is dispersive, with a low frequency cutoff of 1.3 GHz, the propagation time of the driving signal's different Fourier components varies appreciably, as shown in Figure 6.12. As a result, the phase relationship among the various amplitudes changes along the length of the waveguide, even though there relative amplitudes do not. The field in the wave guide five meters upstream of the cavity is shown in Figure 6.13. Note its increased breadth and decreased maximum amplitude relative to the signal at the downstream end of the wave guide. The field at the midpoint and upstream end of the wave guide are shown in Figures 6.14 and 6.15.

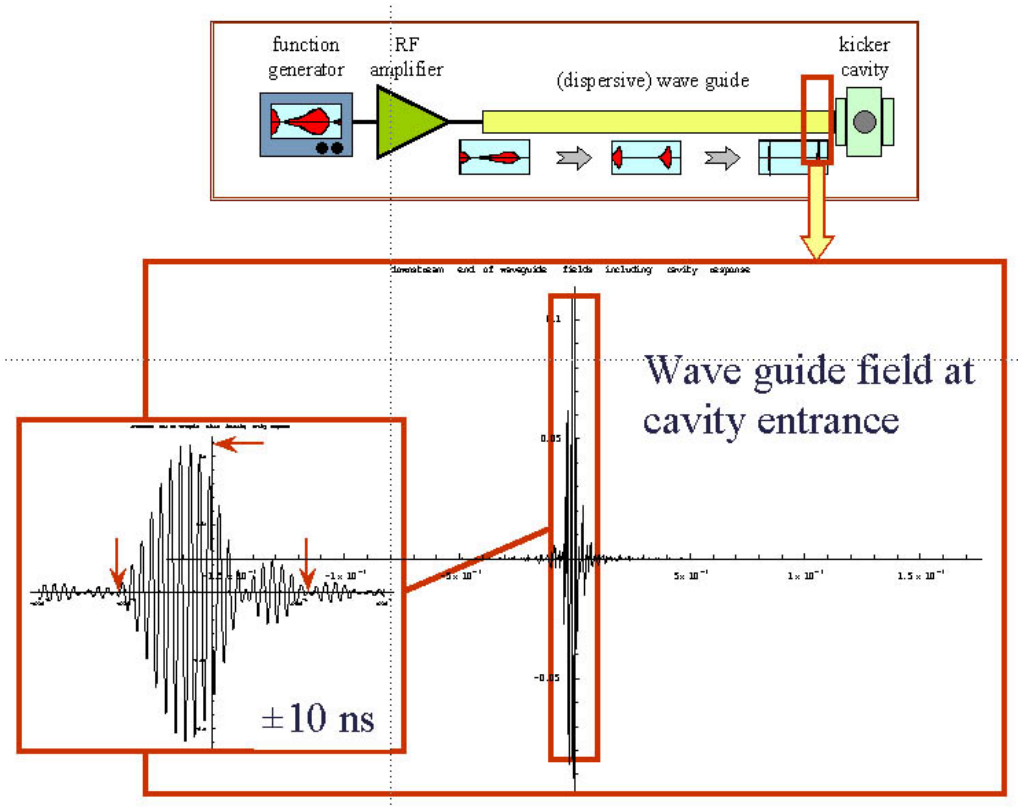

Figure 6.11. Field at downstream end of wave guide. Amplitude, indicated relative to the maximum amplitude inside the RF cavity, has peak value of approximately 0.11. Full scale time range is 20 ns in the inset and approximately 340 ns in the larger figure. Red arrows in the inset indicate arrival times of the kicked bunch in the cavity (at $t = 0$) and the bunches immediately before and after the kicked bunch.

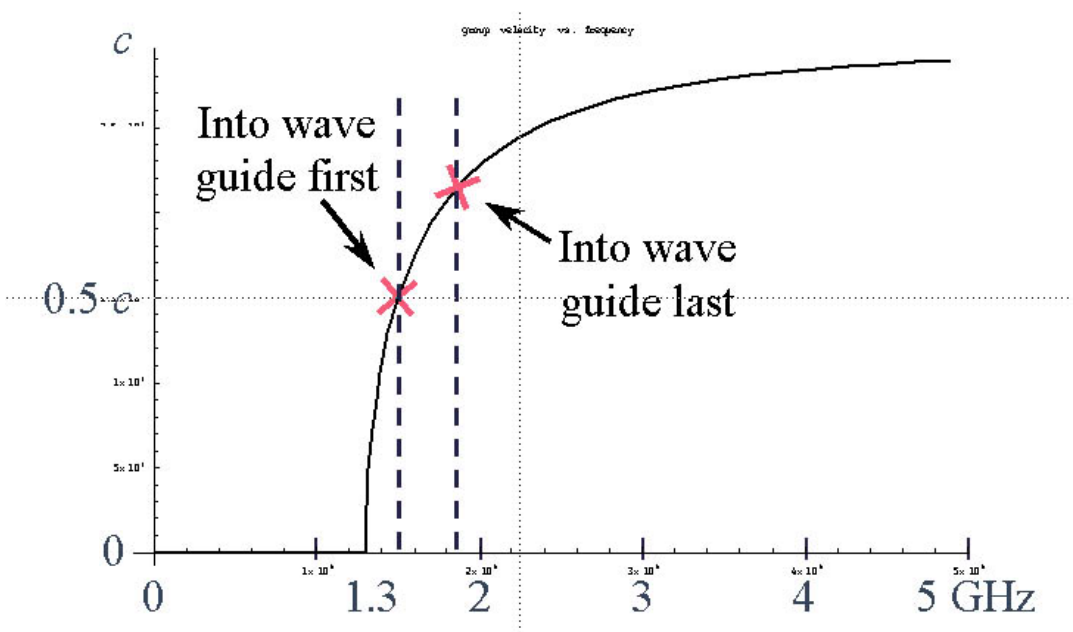

Figure 6.12. Group velocity vs. frequency in the wave guide.

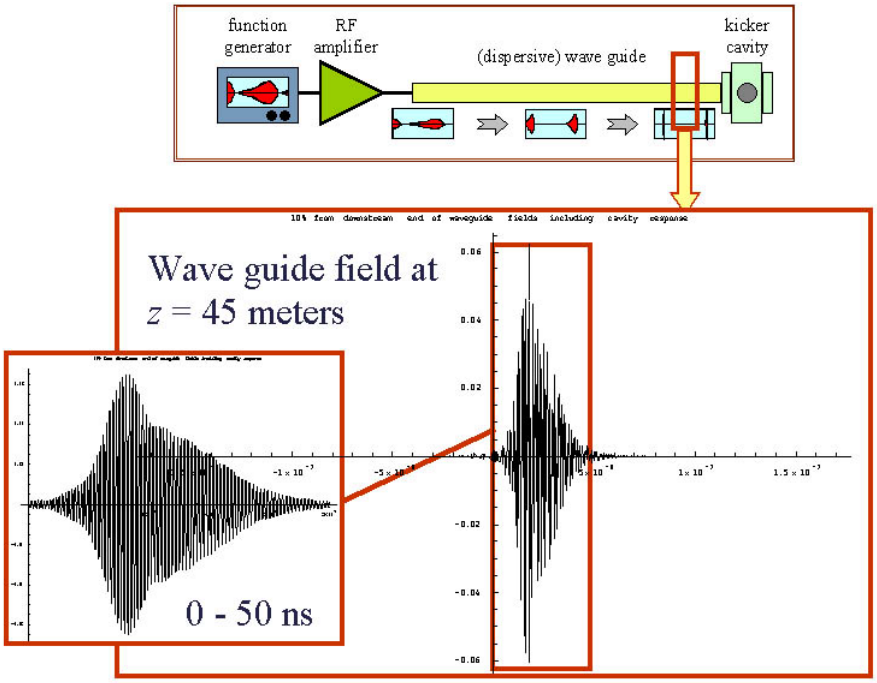

Figure 6.13. Field five meters before the downstream end of wave guide. Amplitude, indicated relative to the maximum amplitude inside the RF cavity, has peak value of approximately 0.6. Full scale time range is 50 ns in the inset and approximately 340 ns in the larger figure.

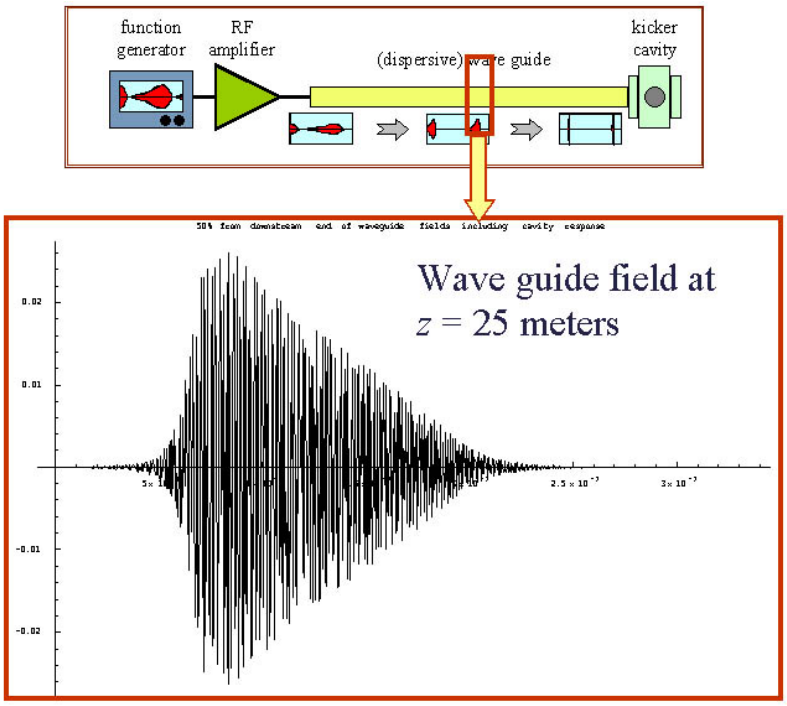

Figure 6.14. Field at the midpoint of the wave guide. Amplitude, indicated relative to the maximum amplitude inside the RF cavity, has peak value of approximately 0.03. Full scale time range is approximately 340 ns.

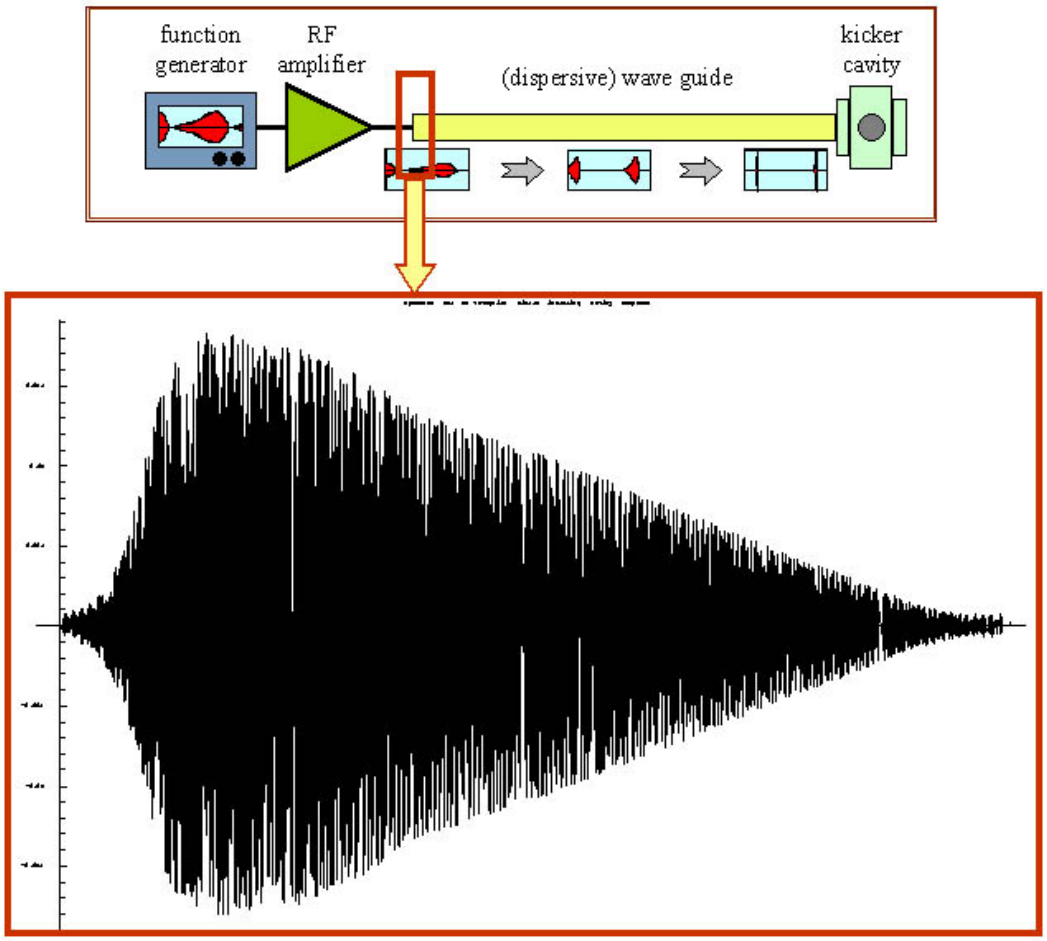

Figure 6.15. Field at the upstream end of the wave guide. Amplitude, indicated relative to the maximum amplitude inside the RF cavity, has peak value of approximately 0.018. Full scale time range is approximately 340 ns.

Cavity Design and RF Power Requirements

We are currently discussing details of possible cavity designs and amplifier schemes with the Fermilab RF group. Rough estimates for power consumption suggest that a 60 kW RF amplifier is necessary; the combination of required bandwidth and power would indicate that a traveling wave tube, rather than a klystron, is necessary.

Stability Considerations

Studies of the various vulnerabilities of the kicker to drifts and errors are in progress. The use of a programmable function generator as a signal source should permit adjustment of the system as components age, though detailed consideration of feedback issues has yet to be done.

The effect of a 0.1% error in cavity Q is shown in Figure 6.16 as a function of bunch number. (The first bunch is kicked, the rest are not.). The vertical scale shows deviation from the ideal impulse, with the strength of a perfect (100 Gauss-m) kicking pulse indicated as 1.000. The maximum allowable error of 0.07 Gauss-m corresponds to 0.0007 on this scale. Note that an error in Q changes the cavity response vs. frequency, effectively inducing an error in the relative amplitudes and phases of the various Fourier components. As can be seen, the maximum permissible Q error is approximately 0.1%.

The effect of a 0.1% (1.647 MHz) mistuning of RF cavity center frequency is shown in Figure 6.17. As before, the vertical scale shows deviation from the ideal impulse with the maximum allowable error corresponding to 0.0007 on this scale. The maximum permissible tuning error is somewhat smaller than this, approximately 1.4 MHz.

Figure 6.18 illustrates the consequences of a 1 mm error in the length of the (50 m long) wave guide. To a great extent, the effect of an error in wave guide length is to induce a timing error in the generation of the kicking pulse at the cavity relative to the passage of the kicked bunch. As a result, the kick error increases quadratically with wave guide length error since the kicking pulse is approximately parabolic in shape.

Figure 6.19 shows the results of a 10 kHz error in wave guide cutoff frequency. Since cutoff frequency depends directly on the waveguide geometry, controlling (or reducing sensitivity to this) parameter may require a certain amount of innovation.

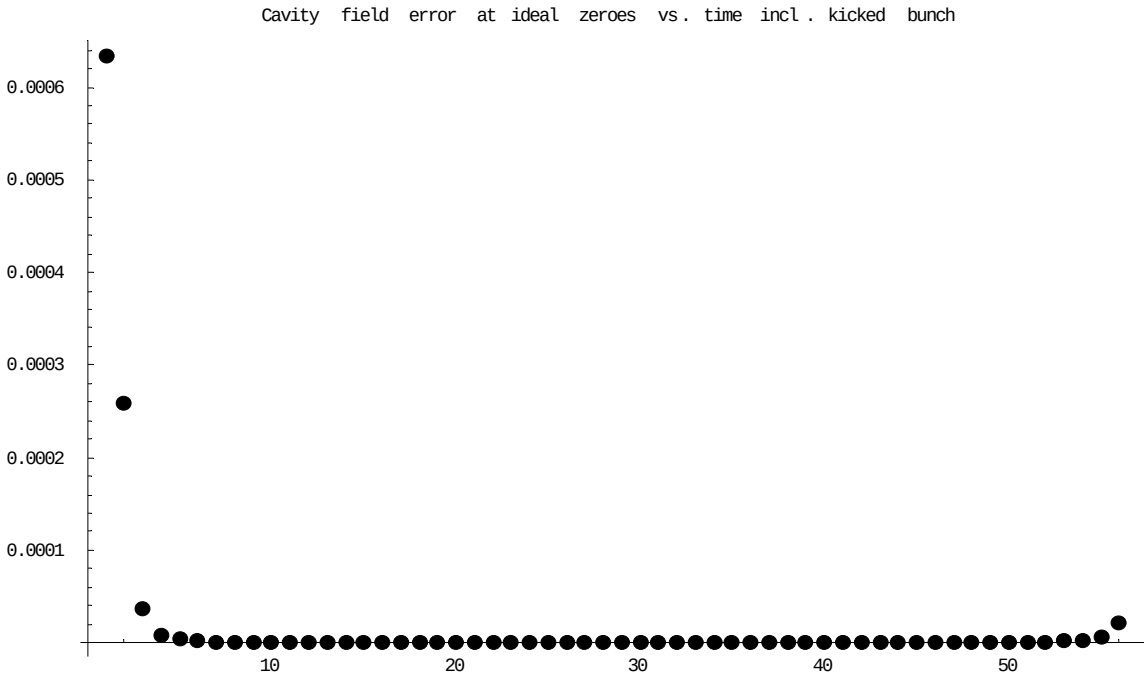

Figure 6.16. Kick error induced by a 0.1% error in RF cavity Q as a function of bunch number. The first bunch is injected/extracted, while others pass through the kicker undeflected. (Maximum allowable kicking error is 0.007 in these units.)

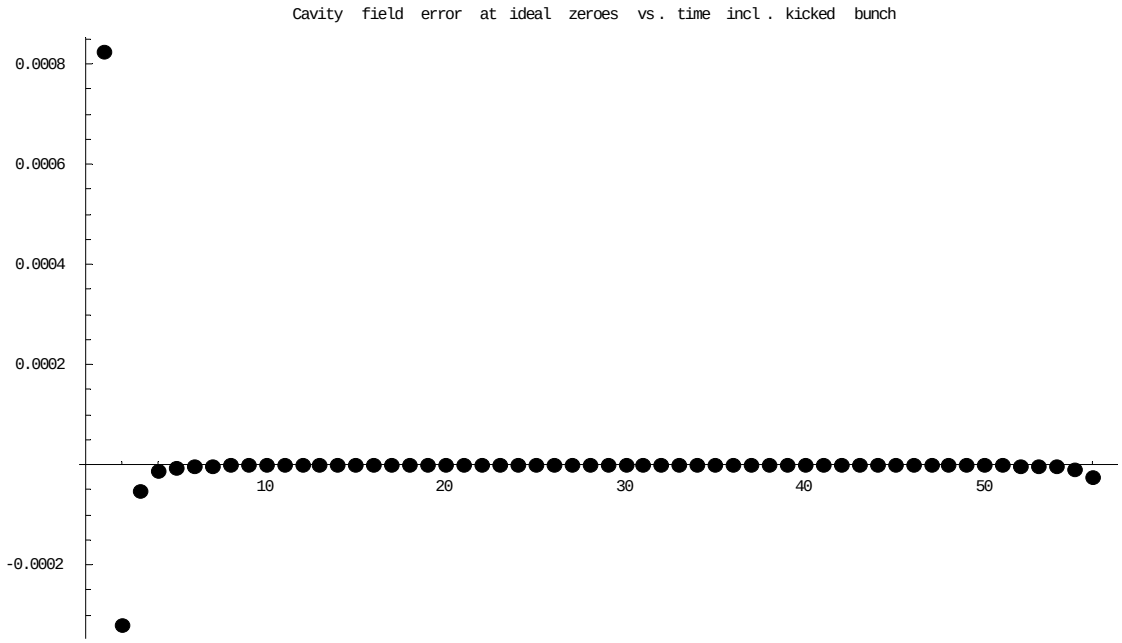

Figure 6.17. Kick error induced by a 0.1% error in RF cavity center frequency as a function of bunch number. The first bunch is injected/extracted, while others pass through the kicker undeflected. (Maximum allowable kicking error is 0.007 in these units.)

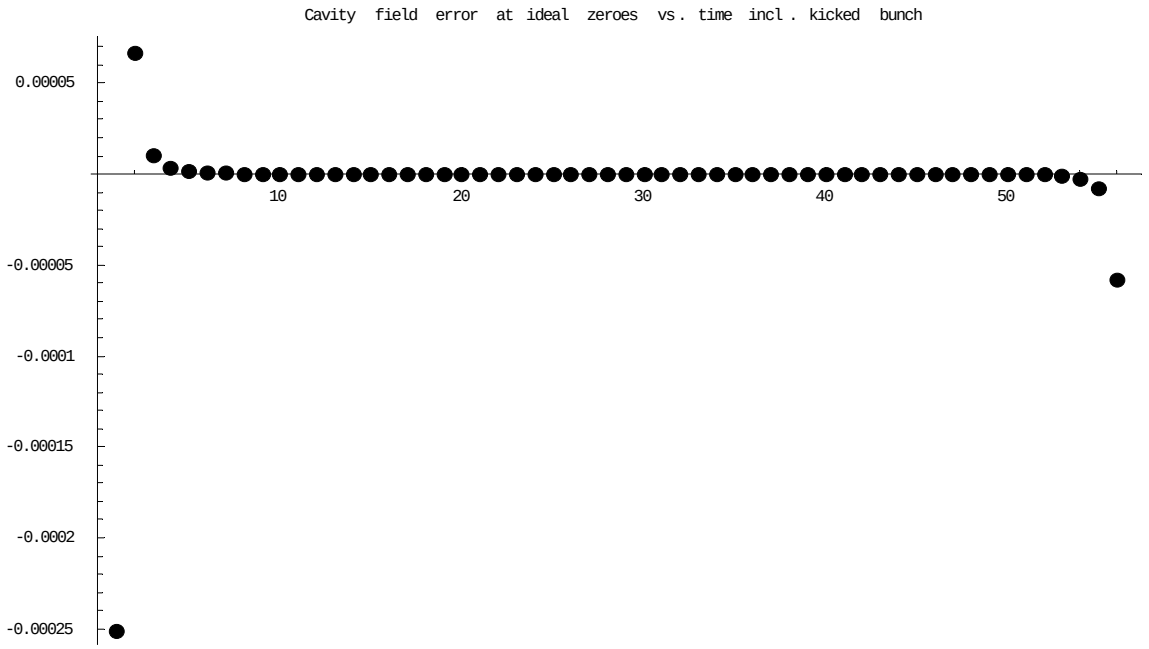

Figure 6.18. Kick error induced by a 1 mm error in wave guide length as a function of bunch number. The first bunch is injected/extracted, while others pass through the kicker undeflected. (Maximum allowable kicking error is 0.007 in these units.)

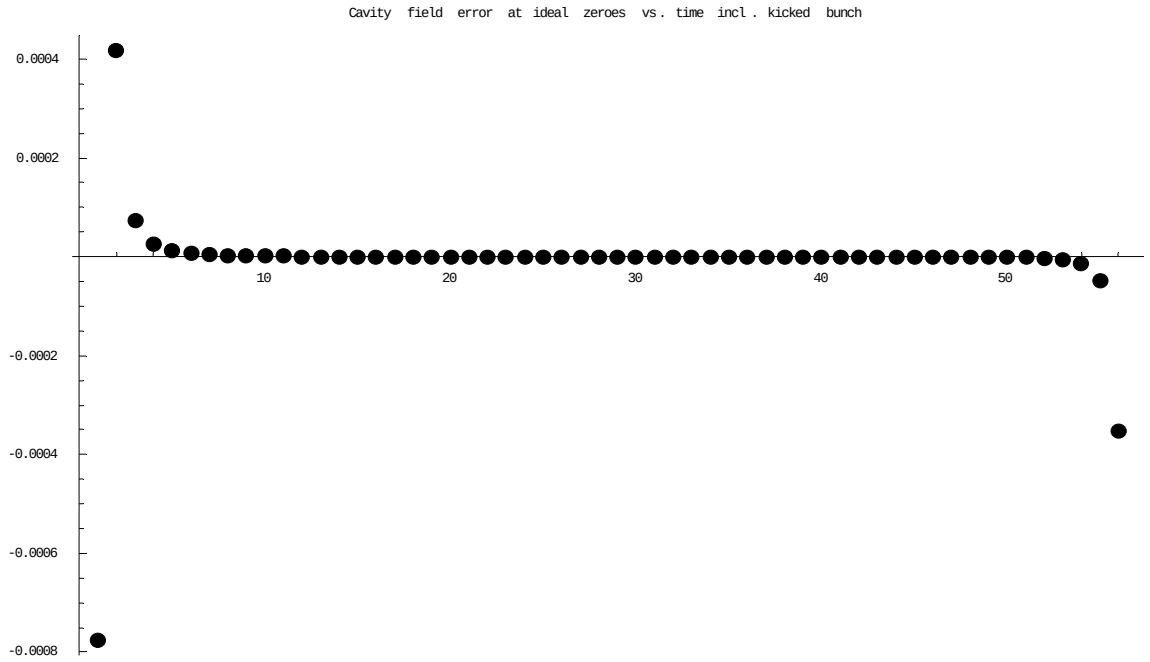

Figure 6.19. Kick error induced by a 10.0 kHz error in wave guide cutoff frequency as a function of bunch number. The first bunch is injected/extracted, while others pass through the kicker undeflected. (Maximum allowable kicking error is 0.007 in these units.)

Studies are in progress.

7. Conclusions

Our investigations of the feasibility of a small ILC damping ring are encouraging, but there is a considerable amount of work that remains to be done. In particular, thorough studies of dynamic aperture and kicking techniques will continue. But our results indicate that it is sensible to pursue, for the time being, studies of both the dog bone and small damping rings. It is likely that a kicker that works in a small ring will also work nicely in the dog bone design. Questions of early commissioning of the damping ring are more simply resolved for the small rings with their independent tunnels.

References

2.1 P. Emma and T. Raubenheimer, *A Systematic Approach to Damping Ring Design,* Phys. Rev. ST Accel.Beams 4:021001, 2001.

2.2 TESLA *Technical Design Report.*

2.3 R. Helm et al., in *Proceedings of the 1973 IEEE Particle Accelerator Conference,* San Francisco, p. 900.

2.4 L. C.Teng, Fermilab Report No. TM-1269, 1984.

2.5 Mark Woodley and Andrzej Wolski, *The NLC Main Damping Ring Lattice,* SLAC-TN-03-031, Feb. 2003.

4.1 TESLA *Technical Design Report* (March, 2001).

4.2 W. Decking and R. Brinkmann, *Space Charge Problems in the TESLA Damping Ring*, Proc. 7th EPAC, Vienna 2000, p.1024.

4.3 M. Blaskiewicz, *Fast Head-tail Instability with Space Charge*, Phys. Rev. ST Accel. Beams, 1, 044201 (1998).

4.4 NLC Design Group, *Zeroth-Order Design Report for the Next Linear Collider,* LBNL-5424, SLAC-474, UCRL-ID-124161, UC-414, May, 1996, chapter 4.

4.5 M.A. Furman and G.R. Lambertson, *The Electron-Cloud Instability in the PEP-II Positron Ring*, Proc. Int. Workshop on Multibunch Instabilities in Future Electron and Positron Accelerators (MBI'97), Tsukuba, KEK, 15-18 July, 1997, KEK Proceedings 97-17 1997, p.170.

4.6 F. Zimmermann, *Accelerator Physics studies for KEKB: Electron Trapping, Electron Cloud in the HER, Closed-Orbit Drift, Horizontal Instability and Tune Shift*, KEKB Commissioning Report, April 2, 2002, and CERN SL-Note-2002-017 AP (2002).

4.7 T.O. Raubenheimer and F. Zimmermann, *A Fast Beam-Ion Instability in Linear Accelerators and Storage Rings,* Phys. Rev. E52, 5487 (1995)

4.8 A.W Chao, *Lecture Notes on Topics in Accelerator Physics*, US Particle Accelerator School at SUNY Stony Brook, New York, June 5-16, 2000.

5.1 TESLA Design Report, chapter 3 (1997).

5.2 TESLA Design Report , chapter 5 (2001).

5.3 A. Wolski, "Alignment sensitivities in ILC Damping Rings", unpublished, August 2004.

5.4 Y. Honda *et al.,* "Achievement of Ultra low Emittance Beam in the ATF Damping Ring, Phys. Rev. Lett.

5.5 R. Brinkmann and J. Rossbach, "Observation of Closed Orbit Drift at HERA", Nucl. Inst. And Meth. A350

5.6 T. O. Raubenheimer, "The Generation and Acceleration of Low Emittance Flat Beams for Future Linear Colliders, Thesis, SLAC-387

5.7 T. O. Raubenheimer, "Emittance Growth due to Beam-Gas Scattering", KEK report 92-7, 1992.

5.8 A. Piwinski, "Intrabeam Scattering with Vertical Dispersion", Proc. SSC Workshop, Ann Arbor, MI, 1983.

6.1. *TESLA Technical Design Report,* http://tesla.desy.de/new_pages/TDR_CD/start.html (March, 2001).

6.2. R. E. Shafer, *Bunch Shapes, Fourier Transforms, and Spectral Power Densities,* http://www.sns.gov/diagnostics/documents/ fdrreview/Laser/BunchShapes1.pdf (March, 2002).

6.3. By writing the cosine as the sum of a pair of complex exponentials, it is evident that the sum over harmonics is just a pair of geometric series:

$$\frac{1}{2}+\sum_{k=1}^{N}\cos\left(k\omega_0 t\right)=\frac{1}{2}+\sum_{k=1}^{N}\frac{e^{ik\omega_0 t}+e^{-ik\omega_0 t}}{2}=\frac{1}{2}\sum_{k=0}^{N}\left[e^{ik\omega_0 t}+e^{-ik\omega_0 t}\right]=\frac{1}{2}\sum_{k=0}^{N}\left(e^{i\omega_0 t}\right)^k+\frac{1}{2}\sum_{k=0}^{N}\left(e^{-i\omega_0 t}\right)^k.$$

The geometric series can be summed in the usual way; reexpression of the result in terms of sines and cosines yields the desired answer.